

Engineering Redox Flow Battery Electrodes with Spatially Varying Porosity Using Non-Solvent-Induced Phase Separation

Citation for published version (APA):

Wan, C. T. C., Jacquemond, R. R., Chiang, Y. M., Forner-Cuenca, A., & Brushett, F. R. (2023). Engineering Redox Flow Battery Electrodes with Spatially Varying Porosity Using Non-Solvent-Induced Phase Separation. *Energy Technology*, 11(8), Article 2300137. <https://doi.org/10.1002/ente.202300137>

DOI:

[10.1002/ente.202300137](https://doi.org/10.1002/ente.202300137)

Document status and date:

Published: 01/08/2023

Document Version:

Publisher's PDF, also known as Version of Record (includes final page, issue and volume numbers)

Please check the document version of this publication:

- A submitted manuscript is the version of the article upon submission and before peer-review. There can be important differences between the submitted version and the official published version of record. People interested in the research are advised to contact the author for the final version of the publication, or visit the DOI to the publisher's website.
- The final author version and the galley proof are versions of the publication after peer review.
- The final published version features the final layout of the paper including the volume, issue and page numbers.

[Link to publication](#)

General rights

Copyright and moral rights for the publications made accessible in the public portal are retained by the authors and/or other copyright owners and it is a condition of accessing publications that users recognise and abide by the legal requirements associated with these rights.

- Users may download and print one copy of any publication from the public portal for the purpose of private study or research.
- You may not further distribute the material or use it for any profit-making activity or commercial gain
- You may freely distribute the URL identifying the publication in the public portal.

If the publication is distributed under the terms of Article 25fa of the Dutch Copyright Act, indicated by the "Taverne" license above, please follow below link for the End User Agreement:

www.tue.nl/taverne

Take down policy

If you believe that this document breaches copyright please contact us at:

openaccess@tue.nl

providing details and we will investigate your claim.

Engineering Redox Flow Battery Electrodes with Spatially Varying Porosity Using Non-Solvent-Induced Phase Separation

Charles Tai-Chieh Wan, Rémy Richard Jacquemond, Yet-Ming Chiang, Antoni Forner-Cuenca,* and Fikile R. Brushett*


Redox flow batteries (RFBs) are a promising electrochemical platform for efficiently and reliably delivering electricity to the grid. Within the RFB, porous carbonaceous electrodes facilitate electrochemical reactions and distribute the flowing electrolyte. Tailoring electrode microstructure and surface area can improve RFB performance, lowering costs. Electrodes with spatially varying porosity may increase electrode utilization and provide surface area in reaction-limited zones; however, the efficacy of such designs remains an open area of research. Herein, a non-solvent-induced phase-separation (NIPS) technique that enables the reproducible synthesis of macrovoid-free electrodes with well-defined across-thickness porosity gradients is described. The monotonically varying porosity profile is quantified and the physical properties and surface chemistries of porosity-gradient electrodes are compared with macrovoid-containing electrode, also synthesized by NIPS. Then, the electrochemical and fluid dynamic performance of the porosity-gradient electrodes is evaluated, exploring the effect of changing the direction of the porosity gradient and benchmarking against the macrovoid-containing electrode. Lastly, the performance is examined in a vanadium RFB, finding that the porosity-gradient electrode outperforms the macrovoid electrode, is independent of gradient direction, and performs favorably compared to advanced electrodes in the contemporary literature. It is anticipated that the approach motivates further exploration of microstructurally tailored electrodes in electrochemical systems.

1. Introduction

Curtailling greenhouse gas emissions driving climate change while meeting societal energy demands is among the grandest challenges confronting humanity.^[1] Despite the unprecedented low costs of harvesting energy from renewables such as solar and wind, their inherent intermittency and unpredictability across multiple time scales from seconds to seasons stymies widespread penetration into the electric grid,^[2] motivating the development of energy-storage technologies.^[3] Electrochemical systems have garnered interest for cost-effectively storing and releasing energy; while numerous battery platforms may be leveraged for this purpose, redox flow batteries (RFBs) have emerged as promising candidates for longer duration energy-storage applications due to their independent energy and power scaling, long operational lifetimes, and improved safety.^[4,5] Despite their promise, adoption of RFB technologies has been limited, in large part, due to their high upfront costs that challenge the stringent economics of grid energy storage.^[6] Accordingly, research efforts have focused on developing new electrolyte formulations

C. T. C. Wan, Y.-M. Chiang, F. R. Brushett
Joint Center for Energy Storage Research
Massachusetts Institute of Technology
Cambridge, MA 02139, USA
E-mail: brushett@mit.edu

C. T. C. Wan, F. R. Brushett
Department of Chemical Engineering
Massachusetts Institute of Technology
Cambridge, MA 02139, USA

 The ORCID identification number(s) for the author(s) of this article can be found under <https://doi.org/10.1002/ente.202300137>.

© 2023 The Authors. Energy Technology published by Wiley-VCH GmbH. This is an open access article under the terms of the Creative Commons Attribution License, which permits use, distribution and reproduction in any medium, provided the original work is properly cited.

DOI: 10.1002/ente.202300137

R. R. Jacquemond, A. Forner-Cuenca
Membrane Materials and Processes
Department of Chemical Engineering and Chemistry
Eindhoven University of Technology
5600 MB Eindhoven, The Netherlands
E-mail: a.forner.cuenca@tue.nl

R. R. Jacquemond
DIFFER - Dutch Institute for Fundamental Energy Research
5612 AJ Eindhoven, The Netherlands

Y.-M. Chiang
Department of Materials Science and Engineering
Massachusetts Institute of Technology
Cambridge, MA 02139, USA

containing lower-cost or higher-performance redox couples,^[7,8] as well as advancing more efficient cell and stack designs.^[4,9,10]

An effective strategy to reduce RFB system costs is to improve the areal power density. Tailoring the properties of core components (i.e., electrodes, membranes, flow fields) can reduce kinetic, Ohmic, and transport resistances, thus augmenting overall reactor output.^[11] To this end, porous carbon electrodes support multiple critical functions in the cell (and stack). Electrolyte travels through the flow field and is transported into the porous electrode, within which electrochemical reactions occur at the electrode–electrolyte interfaces. Therefore, the arrangement, connectivity, and volume of pores (i.e., the microstructure) affect the electrolyte distribution throughout the electrode, and the electrode surface area, composition, and topology dictate local reaction rates. Commercial porous electrodes employed in RFBs typically comprise polyacrylonitrile- (PAN) or Rayon-derived micrometric fibers arranged into different freestanding structures.^[12] While functional, as-received electrodes exhibit poor catalytic rates for state-of-the-art aqueous RFB couples, necessitating post-process surface modifications, *via* thermal,^[13–15] electrochemical,^[16,17] or alternative routes,^[18] to generate favorable surface chemistries and to increase electrochemically accessible surface area. Furthermore, as many leading porous electrodes used in RFBs were originally designed as gas diffusion layers (GDLs) for polymer electrolyte membrane (PEM) fuel cells (PEMFCs),^[19] their microstructure may not be optimal for the liquid-phase reactions they underpin.^[12,20] Thus, optimizing the surface properties and porous structure of these electrodes offers opportunities for dramatic improvements in electrochemical and fluid dynamic performance.^[21]

A growing body of work has illuminated the importance of mass transport in the energy-efficient operation of high-power-density redox flow cells. The microstructural diversity and post-process tunability of commercial electrodes is limited by available offerings. Consequently, approaches to develop bottom-up fabricated scaffolds have gained traction as they enable control over the design of pore shapes and morphologies, broadening the available pore network space and supporting the establishment of microstructure–function–performance relationships. To date, the majority of these efforts have focused on the research and development of fibrous electrospun materials.^[22] These works have shown that aligned fiber arrangements and hierarchical and ordered carbon-fiber electrodes can enable large performance improvements by balancing kinetic and transport properties.^[23–25] These experimental advances have occurred in tandem with efforts to quantify the anisotropy of the 3D electrospun structures,^[26] develop mass-transfer correlations of anisotropic materials using multiphysics simulations,^[27] and screen microstructures and electrode properties *via* pore-scale computational approaches (i.e., pore network modeling,^[28,29] lattice Boltzmann methods,^[30,31] and algorithmic optimization^[32]). Collectively, these results suggest that hierarchical porous structures with locally anisotropic channels can address mass-transport limitations while providing ample surface area for the redox reactions.

Another approach to improving electrode performance is to tune the microstructure (i.e., spatially varying porosity from the flow field to the separator) such that the electrolyte is directed to reaction-limited zones or to areas with increased surface area.^[33] This strategy is a departure from conventional RFB

electrodes characterized by macrohomogeneous porosity. Indeed, electrochemical technologies with gaseous reactants or products (e.g., PEMFCs) contain multiple transport layers (e.g., GDL, microporous layer, catalytic layer), each with distinct microstructure, surface chemistry, and wettability to support the efficient operation of the device. Porosity gradients have also been explored to reduce Ohmic resistances in lithium-ion batteries,^[34] augment current densities in PEMFCs,^[35] and reduce mass-transport overpotential in PEM electrolyzers. The desire for a porosity gradient in RFBs arises from the tension between providing surface area in reaction-limited zones while also supplying electrolyte uniformly throughout the electrode matrix, which require diametrically opposing porosities. In a porous electrode, current distribution forms as a function of location within the electrochemical cell stemming from ionic current limitations near the membrane–electrode interface. A further complication in RFBs is the presence of convection, affecting mass transport from the bulk electrolyte to the electrode surface. Thus, supplying electrolyte to this limiting region by lowering the porosity is one strategy; increasing the electrode surface area near the membrane is another. Ultimately, tuning the porosity gradient is posited to enable more uniform electrolyte distribution while also providing sufficient surface area in the necessary regions.

The effect of porosity profile on all-vanadium redox flow battery (VRFB) performance has been observed experimentally in several recent studies, finding generally that decreasing porosity from the flow field to membrane could outperform baseline macrohomogeneous materials by distributing electrolyte flow into the electrode while providing higher surface area near the reaction-limited membrane.^[36,37] Meanwhile, Loretz *et al.* found that decreasing electrode porosity outwardly from the membrane in at least one or both electrodes decreased contact resistance.^[38] The inability to accurately measure varying velocity and pressure fields within RFB electrodes motivates modeling work to explore the design space in a more systematic fashion. Simplified 2D multiphysics models for VRFBs have been leveraged to evaluate different electrode porosity profiles from the flow field to the membrane^[39] for fixed inlet flow or fixed pressure difference,^[40] vertically and diagonally varying porosity have also been simulated.^[41] Ultimately, these studies demonstrate that the best combination of electrode porosity gradients depends on certain parameters (e.g., porosity variation amplitude, electrode thickness, flow rate) and the desired metric (i.e., energy, pumping, or system efficiency). While these pioneering works shed light on the field, consensus has not yet been reached on the optimal direction or features of the porosity profile, which appears to be nuanced and dependent on a multitude of desired operating conditions (e.g., flow rate, current density), redox electrolyte pairings each having distinctive reaction rates and electrolyte properties (i.e., viscosity, density, and conductivity), and rank-ordered performance metrics (e.g., energy, pumping, or overall system efficiency). Determining the optimal directionality, shape, magnitude, average porosity, and local porosity of the gradient for each unique redox couple and electrolyte is still an active area of research. Furthermore, developing a versatile method of synthesizing the optimal porosity gradient compatible with scalable manufacturing capabilities is of commercial relevance.

In this work, we synthesize porous carbon electrodes with monotonic porosity gradients, characterize their physical and chemical properties, and evaluate their performance in redox flow cells. We recently developed a new class of electrode microstructures through a facile, versatile, and potentially scalable process known as non-solvent-induced phase separation (NIPS).^[42,43] In this process, a single-phase mixture of scaffold-forming polymers dissolved in a solvent is driven into two phases by a non-solvent, yielding a scaffold which can subsequently be thermally annealed into a carbonaceous and electrochemically active material. These microstructures, under the parameters sets in our previous work, show clear polydisperse pore distributions containing large pores (termed macrovoids) leading into small pores (termed microvoids) that balance electrochemical and fluid dynamic processes within the electrodes.^[42,43] Additionally, these architectures hold promise to enable high power density VRFBs.^[43] Here, we advance a NIPS method to generate materials with spatially varying porosity in the through-plane by introducing a pre-immersion step in the solvent (here, *N,N*-Dimethylformamide [DMF]) prior to exposure to the non-solvent, buffering the phase-separation process, delaying demixing, and, thus, preventing macrovoid formation. We systematically characterize the surface chemistry and physical properties of the porosity gradient and juxtapose them to a macrovoid-containing structure synthesized with the same polymer and solvent formulations, finding minimal differences in physicochemical characteristics. Subsequently, we employ single-electrolyte flow-cell measurements with the porosity-gradient electrode to compare the effect of changing the direction of the porosity gradient from the flow field to the membrane on the performance, and further benchmark those results to the macrovoid-containing structure. These efforts culminate in galvanostatic cycling and discharge polarization of a VRFB full cell. Ultimately, our aim is to illustrate opportunities for the development of high-performance porosity-gradient electrodes for RFBs.

2. Results and Discussion

2.1. Synthesis Procedure

We first provide a brief description of the generic NIPS process of forming membranes, and then hypothesize the mechanism driving the formation of the porosity-gradient electrode. The NIPS process refers to the controlled precipitation of a dissolved polymer in a solvent by immersing the polymer–solvent mixture into a non-solvent bath, resulting in solvent–non-solvent exchange (i.e., demixing) and phase separation into scaffold-forming polymer rich and pore-forming polymer-poor phases.^[44–47] Accordingly, the microstructure of membranes synthesized from NIPS is the result of an interplay between thermodynamic interactions and transport properties of the scaffold-forming polymer (PAN), additional pore-forming additives (polyvinylpyrrolidone [PVP]), solvent [DMF], and non-solvent [water]). While a wide range of morphologies can be derived using the NIPS process, prior membrane characterization work has led to the identification of two mechanisms which result in two distinct membrane morphologies: I) instantaneous demixing to yield finger-like microstructures, and II) delayed demixing to yield sponge-like microstructures.^[44,48] In the first case, macrovoid-containing structures have been observed when demixing is

rapid; the formation of macrovoids frequently coincides with hydrodynamic flows, and depends on the solvent–non-solvent miscibility.^[47,49–51] Several theories for macrovoid formation have been proposed, including diffusion-based mass-transfer mechanisms where the faster onset of precipitation leads to macrovoids,^[49,52,53] or mechanical stresses at the solution–bath interface that initiate local surface instabilities and cause rupture points acting as nucleation sites for macrovoid formation followed by non-solvent convective flows into the blend.^[44,54,55] although the exact mechanism is the subject of debate.^[46,47,51] Regardless, the morphology of this class of materials is typically characterized by a thin top layer with large finger-like pores extending through the membrane thickness. In the second case, it is posited that slow precipitation from delayed solvent–non-solvent exchange leads to the formation of macrovoid-free, sponge-like structures with more uniform porosity.^[46,47] While the exact mechanisms of NIPS are still debated, generalizable principles indicate that less miscible solvent–non-solvent pairing, more compatible polymer–solvent coupling, and high polymer concentration/viscosity tend to favor the formation of sponge-like structures.^[44,46,47,49,55] Accordingly, numerous factors can influence the resulting NIPS microstructure, including, but not limited to, the relative ratio of polymers, choice of solvent and polymers, total solids concentration, bath/casting temperature, and various additives, impacting the phase-separation process and interactions on different length scales.^[43,46,47]

Here, PAN is the scaffold former, PVP is the pore former, DMF is the solvent, and water is the non-solvent. We have previously shown the formation of macrovoid structures at various polymer concentrations, solvents, and bath temperatures.^[43] These materials from our previous work displayed polydisperse pore sizes with finger-like internal microstructure; further, the dense skin layer which adds resistance to the electrode was removed using vapor-induced phase separation (VIPS) from the ambient environment prior to NIPS.^[56] We sought to synthesize a macrovoid-free porosity-gradient electrode using the same solution composition, as the reagents are common precursors used in the development of carbonaceous materials and would thus be compatible with existing scalable supply chains and infrastructures.^[20,21] To remove the macrovoids, we employ a solvent buffer layer by first immersing the casted polymers into a DMF bath for ≈ 5 s, and then transferring the assembly to the water bath to phase separate overnight. The DMF bath improves local component miscibility at the interface of the casted solution and slows down non-solvent penetration into the casted polymer solution within the mold. Furthermore, we hypothesize that the addition of DMF prevents the formation of macrovoid-nucleating seeds, which occur due to fluctuations in polymer/solvent/non-solvent concentrations near the bath/solution interface, by smoothing the rapid change in non-solvent concentration, further inhibiting macrovoids. Thus, without changing the formulation, we successfully synthesize a macrovoid-free electrode with a porosity gradient; **Figure 1** shows the differences in the NIPS process and resulting microstructure between a representative macrovoid structure without the pre-buffering, and a representative porosity-gradient structure with pre-buffering. Based on previous literature, we hypothesize that the observed increasing porosity from the bath–film interface to the film–mold interface spontaneously forms as a result of staggered

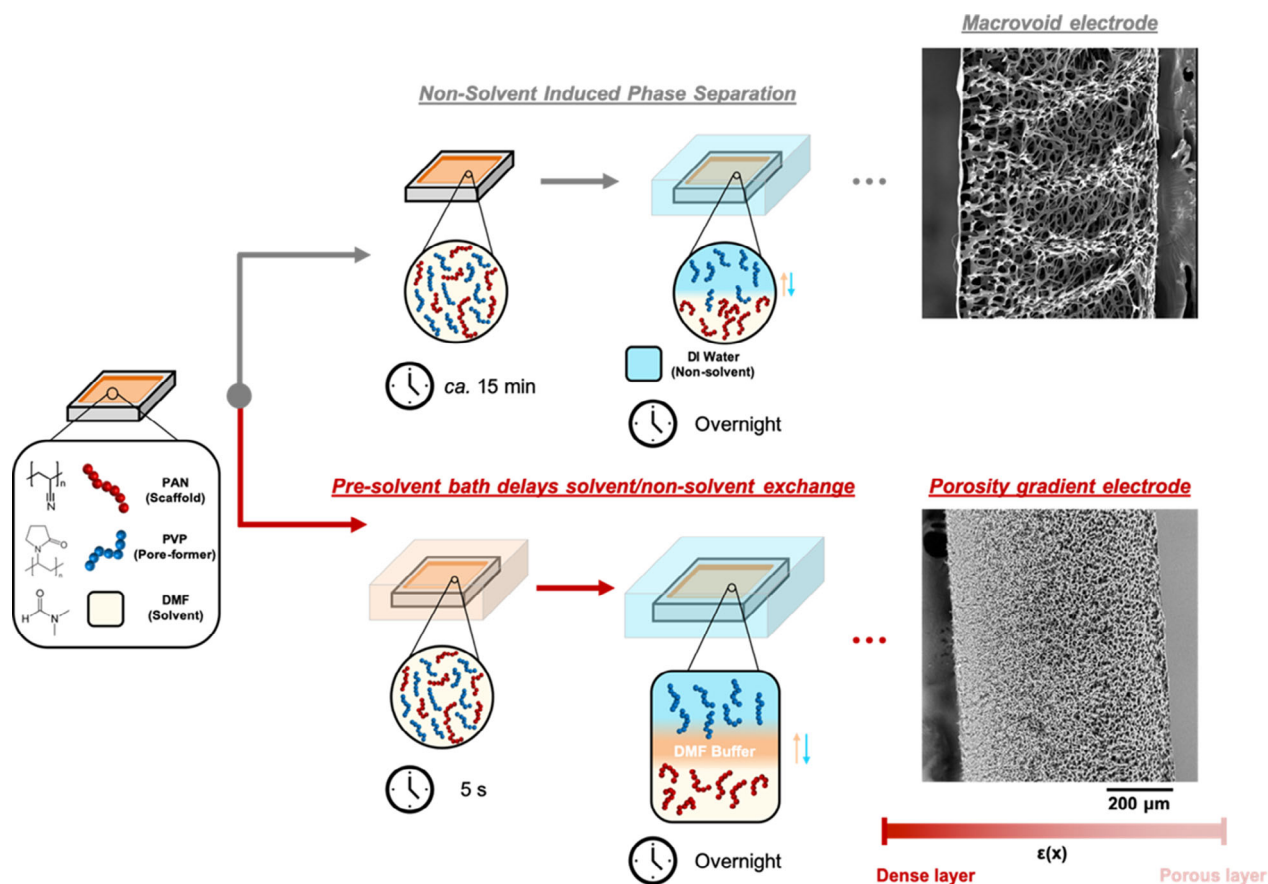


Figure 1. Schematic of the phase-separation process to yield macrovoid-free electrodes with through-plane porosity gradients. The mixture of polyacrylonitrile (PAN), polyvinylpyrrolidone (PVP), and *N,N*-dimethylformamide (DMF) is casted into an aluminum mold, where it is first submerged in a DMF bath for ≈ 5 s, then transferred immediately into a deionized (DI) water bath and left to phase-separate overnight. The pre-DMF immersion bath creates a buffer zone at the top of the mold where local DMF concentration is higher, thus suppressing rapid phase separation through the depth of the polymer solution. The result is a macrovoid-free electrode with spatially varying porosity from the denser layer (DL) formed at the bath/mold interface to the porous layer (PL) formed at the polymer/mold interface.

precipitation pathways through the film thickness.^[47,57] Specifically, in sponge-like membranes, the casted film surface first undergoes rapid solvent–non-solvent exchange and polymer coarsening, leading to the formation of smaller pores at or near the surface. This denser layer (DL) subsequently restricts solvent–non-solvent exchange further into the casted solution, resulting in a slower rate of precipitation and progressively larger pores formed.^[57] Generally, the porosity-gradient electrodes were thinner than their macrovoid counterpart as measured using a dial thickness gauge, with thicknesses of 468.3 ± 21.7 and $575.5 \pm 11.2 \mu\text{m}$, respectively. We posit the $\approx 18.6\%$ reduction in thickness for the porosity-gradient electrode when compared to the macrovoid electrode despite casting into the same mold geometry stems from the first immersion into the DMF bath prior to non-solvent intrusion, lowering the local polymer concentration and viscosity at the bath–polymer interface. Here, we elect to focus on single formulation, specifically $0.18 \text{ g polymer mL}^{-1}$ of DMF solvent with a PAN:PVP mass ratio of 2:3 casted at room temperature ($\approx 21^\circ\text{C}$), which corresponds to the polymer blend with the lowest solids content in our prior work (16 wt% of polymer),^[43] as higher solids contents formed materials with permeabilities insufficient to support liquid flow without experimental challenges such

as electrolyte leaking (see Figure S1, Supporting Information, for SEMs of porosity-gradient materials from polymer blends with higher solids content synthesized using the same approach).

2.2. Microstructural and Physicochemical Characterization

2.2.1. Image Analysis of Porosity-Gradient Microstructure

Next, we characterize the microstructure of the resulting porosity-gradient material. Scanning electron microscopy (SEM) of the porosity-gradient electrode is shown in **Figure 2a**, revealing a cross section free of macrovoids with monotonically varying pore size through the electrode thickness (i.e., the *z*-axis). We quantify the porosity profile as a function of position by SEM image analysis. Full details of the procedure can be found in the Experimental Section. Briefly, the micrograph is first binarized *via* a thresholding process to generate the image with black and white pixels shown in **Figure 2b**. The average gray values along the *y*-direction (in-plane) as a function of the *z*-axis are determined and fit to an exponential with an offset, yielding $GV(z)$, representing the solid matrix profile, which is then transformed to determine the average porosity, $\epsilon(z)$, using the relation

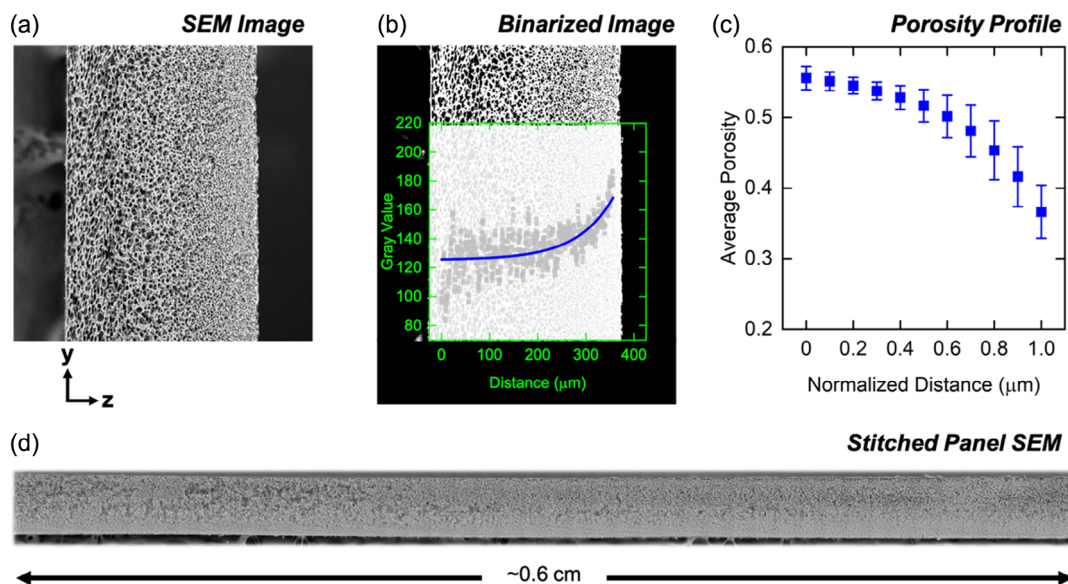


Figure 2. Scanning electron microscopy (SEM) and image analysis of cross-sectioned electrode. a) SEM of the electrode without post-processing. b) Binarized version of the SEM image using thresholding. The gray value is determined by taking the average of the black and white pixels as a function of the position in the y -plane. c) The average porosity is determined as a function of normalized distance across three cross sections of independent samples ($N = 3$). d) Stitched SEM across a broad length of the electrode, showing no macrovoid formation at the sub-centimeter scale.

$\epsilon(z) = 1 - \frac{GV(z)}{255}$. Here, 255 is the maximum value on this scale and corresponds to the solid phase. The compiled porosity profile as a function of normalized distance averaged across three independent samples is shown in Figure 2c. Coincidentally, the porosity profile in Figure 2c is strikingly similar to the optimized electrode porosity profile proposed for performance improvement based on porous electrode theory in Li-ion batteries by Ramadesigan et al.,^[34] suggesting potential for these materials in electrochemical systems aside from RFBs. We note that because the binarization procedure can be subject to variation, the averaged porosity profile should be considered as qualitative and is useful as a general description of the profile achieved using DMF buffering during NIPS. Nevertheless, the results reveal a nonlinear porosity profile with a gradient from a denser region formed at the bath/polymer interface to a more porous region formed at the polymer/mold interface. It is important to note that porosities estimated through mercury intrusion porosimetry (MIP) and density measurements are 0.79 and 0.89, respectively. While both measurements are also prone to inaccuracies, they reveal substantially higher porosity compared to the porosity determined using image analysis. The discrepancy could result from internal porosity within the seemingly solid portion of the electrode, or because out-of-plane solids are included in the analysis of the 2D cross section. To analyze the pore-size distribution (PSD) of the porosity-gradient electrodes, we perform MIP, shown in Figure S2, Supporting Information. The MIP results corroborate the SEM images regarding the characteristic pore-size ranges, as the porosity-gradient electrode exhibited 1–5 μm pores with a peak at $\approx 3 \mu\text{m}$, significantly smaller than the range of pores sizes for the macrovoid-containing electrodes, which has an average pore size ranging from ≈ 25 –45 μm . Lastly, to extend the field of view of the porosity-gradient material, we

performed stitched panel SEM, enabling construction of a wide lens $\approx 0.6 \text{ cm}$ view of the sample (Figure 2d). The stitched panel micrograph reveals that the porosity gradient remains visible throughout the entire electrode, and furthermore, no macrovoids were formed during the phase-separation process. Altogether, the image analysis demonstrates the robustness of the modified NIPS synthesis technique to procure macrovoid-free electrodes with exponentially decaying porosity profiles.

2.2.2. Physicochemical Properties of Electrode Materials

The electrode surface chemistry and functional groups are critical in augmenting or inhibiting various electron-transfer processes of relevance to RFBs.^[58–60] Thus, we next compare the surface chemistry and physical properties of both porosity-gradient and macrovoid structures. The labeling convention for the electrodes is as follows: G stands for gradient, the number refers to the total polymer solids content as a percentage, and bottom or top refers to location of the membrane when casted in the mold. For the macrovoid-containing electrode, DMF stands for the solvent and the number again refers to the total polymer solids content as a percentage. To identify the surface chemistry and binding environments of the materials, X-ray photoelectron spectroscopy (XPS) was performed, and survey scans of the bottom and the top of the porosity-gradient material were compared to the macrovoid material (Figure 3a). A breakdown of the quantities of oxygen and nitrogen functionalities is shown in Figure 3b. As expected, XPS demonstrates that the electrodes possess near-identical elemental compositions, as they were produced from the same reagents, mixed in identical formulations, and annealed under the same processing conditions. Based on the XPS survey scan, the electrode materials were mostly carbon, G16_Bottom

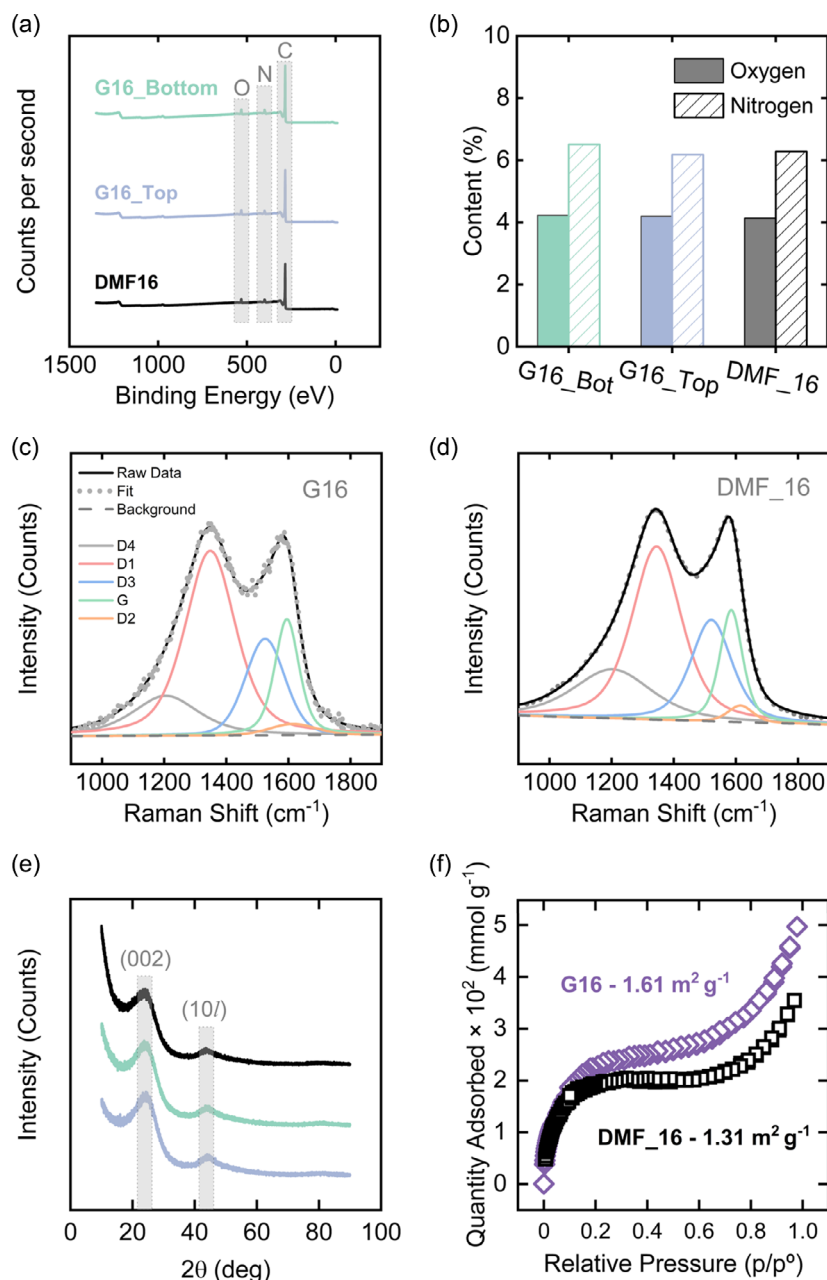


Figure 3. Characterization of physicochemical properties of porosity-gradient and macrovoid-containing electrodes. a) X-ray photoelectron spectroscopy (XPS) survey scans and b) quantification based on atomic percentage for the G16_Bottom, G16_Top, and DMF_16 electrode. Regions of the survey scan corresponding to C, N, and O are shaded in grey and labeled. Detailed and deconvoluted spectrums of the high-resolution C, N, and O scans can be found in Figure S3, Supporting Information. c) Deconvoluted Raman spectra to determine the D and G bands of the porosity-gradient and d) DMF_16 electrodes. The spectra were deconvoluted from a range of 900–1900 cm^{-1} into the D4, D1 (D), D3, G, and D2 bands through mixed Gaussian and Lorentzian curves. A summary of the peak locations, widths, and relative intensities of the D and G bands are provided in Table S2, Supporting Information. e) Comparison of the X-ray diffraction (XRD) patterns for the DMF_16, G16_Bottom, and G16_Top. The (002) and (10 L) crystallographic planes are shaded grey in the diffractograms. f) Ar-gas physisorption of G16 and DMF_16 electrodes, with surface areas determined from Brunauer–Emmett–Teller (BET) analysis shown in the figure. All trials were performed once ($N = 1$).

(≈ 89.3 at%), G16_Top (≈ 89.6 at%), and DMF_16 (≈ 89.6 at%). All samples displayed similar amounts of oxygen and nitrogen functionalities; specifically, G16_Bottom contained ≈ 4.2 at% oxygen and ≈ 6.5 at% nitrogen, G16_Top contained ≈ 4.2 at% oxygen and ≈ 6.2 at% nitrogen, and DMF_16 contained ≈ 4.1 at%

oxygen and ≈ 6.3 at% nitrogen. The presence of both oxygen and nitrogen functionalities are expected because of the maximum carbonization temperature (1050°C) used for electrode synthesis; higher annealing temperatures would increase the degree of carbonization and remove the heteroatoms. Further analyses and

proposed deconvolutions of the high-resolution C1s, N1s, and O1s spectra can be found in Figure S3 and Table S1, Supporting Information. In sum, the XPS results indicate that the all synthesized electrodes possess substantially similar surface chemistry; furthermore, the surface chemistry of the porosity-gradient electrode does not appear to vary, at least at its two outer surfaces, and all electrodes contain oxygen and nitrogen functional groups that could influence redox processes. This analysis also suggests that any discrepancies in electrode performance (*vide infra*) cannot readily be correlated to differences in surface properties but is rather attributed to microstructural features of the porous electrodes effecting the internal electrolyte transport rate.

We next quantify the degree of graphitization and defects in the carbon bonding environments at or near the electrode surfaces *via* Raman spectroscopy as such features have been posited to impact electrochemical performance.^[61] Based on the XPS data indicating amorphous carbons, we anticipate an array of vibrational states arising from the sp³-type bonds.^[62,63] Thus, we seek to compare the Raman spectra of the porosity-gradient electrode to the macrovoid electrode. Figure 3c,d shows that both materials exhibit broad peaks at the G band ($\approx 1590\text{ cm}^{-1}$) and D band ($\approx 1347\text{ cm}^{-1}$). The G band corresponds to a highly ordered graphite-like structure and C–C-stretching vibration, whereas the D band corresponds to a disordered graphitic structure.^[64] Both materials exhibit a broad D peak, indicating more defects and amorphous carbon, with short-range-ordered domains. Again, this intermediate degree of graphitization is expected given that the maximum temperature used during carbonization (i.e., 1050 °C) is lower than the temperature often used in commercial electrode synthesis (up to 1400 °C).^[65,66] To quantify the degree of disorder, the Raman spectra were deconvoluted into five bands, using a mixed Gaussian and Lorentzian fit: D4 ($\approx 1204\text{ cm}^{-1}$), D1 ($\approx 1347\text{ cm}^{-1}$), D3 ($\approx 1523\text{ cm}^{-1}$), G ($\approx 1590\text{ cm}^{-1}$), and D2 ($\approx 1615\text{ cm}^{-1}$).^[67,68] From the fitted distributions of the bands, we use the ratio of the D1-band intensity to the G-band intensity (often denoted as the I_D/I_G ratio) to describe the degree of disordered defects to graphitized bonds.^[67,68] While informative, the I_D/I_G ratio is sensitive, subject to the parameters used to fit the data, and may vary depending on the total number of peaks used.^[69] The I_D and I_G locations, widths, and intensity ratios for the electrode surfaces are summarized in the Table S2, Supporting Information. Briefly, both the G16 and DMF_16 exhibit similar I_D/I_G ratios of 1.59 and 1.55, respectively, indicating the presence of vibrational modes corresponding to disordered defects in addition to graphitized bonds. The similarity in Raman spectra between the porosity-gradient and macrovoid-containing electrodes suggests similar surface defect quantity and identity in each material. We probe the crystallinity of the electrode surfaces by comparing their X-ray diffraction (XRD) patterns. As shown in Figure 3e, diffractograms for G16_Bottom, G16_Top, and DMF_16 are nearly indistinguishable, with broad peaks at $2\theta = \approx 24.1^\circ$ and $\approx 44.4^\circ$, corresponding to the (002) and (10 *l*) atom planes. The d-layer interspacings are estimated as 3.68 Å for G16_Bottom, 3.67 Å for G16_Top, and 3.69 Å for the DMF_16 electrode, as determined by Bragg's equation applied to the 2θ location of the peak corresponding to the (002) plane.^[70] The similarities between the diffractograms and d-layer interspacing further demonstrates the uniformity in crystallinity for the different electrode surfaces.

Lastly, we approximate the specific surface area (SSA) of the electrodes using argon (Ar) physisorption; the isotherms of each electrode are shown in Figure 3f. We note that these measurements can be sensitive especially when considering that nonthermally treated electrode interfaces tend to have smoother surfaces that are nontrivial to estimate.^[15] We use Ar as the adsorbing gas, as it is considered to be more reliable than N₂ as a consequence of its minimal specific interactions with surface polar groups.^[15,71] We find that the G16 electrode exhibited a larger Brunauer–Emmett–Teller (BET) surface area of $1.61\text{ m}^2\text{ g}^{-1}$ relative to that of the DMF_16, which had a smaller BET surface of $1.31\text{ m}^2\text{ g}^{-1}$; this is in agreement with the reduced porosity observed in MIP and SEM of the electrodes. The Ar-physisorption indicates that the G16 electrodes have a $\approx 23\%$ higher SSA than the DMF_16 electrode, although we highlight that the surface areas observed here are on the same order of magnitude, and smaller than SSAs reported for thermally oxidized substrates (i.e., 40–167 $\text{m}^2\text{ g}^{-1}$) that have been employed for use in RFBs.^[15,72] We note that the SSA here should be considered as a comparative measure, as alternative gases or gas mixtures can yield different values. To estimate the electrochemically active surface area (ECSA), which may be more representative of the active surface area available for electrochemical reactions, we perform electrochemical double-layer capacitance (EDLC) on the porosity-gradient materials in the single-electrolyte configuration, varying the direction of the porosity gradient (*vide infra*). We refer to the case where the porosity increases from the flow field to the membrane as G16_PLM, where PLM stands for “porous layer towards the membrane,” and we refer to the case where the porosity decreases from the flow field to the membrane as G16_DLM, where DLM stands for “dense layer towards the membrane.” Representative curves and further explanation of the methodology is provided in Figure S4 and Section S5, Supporting Information. Based on the EDLC measurements, we estimate SSAs of the G16_PLM and G16_DLM to be 2.88 ± 0.36 and $2.80 \pm 0.87\text{ m}^2\text{ g}^{-1}$, respectively. For DMF_16, we previously determined an SSA estimated through EDLC of $0.84 \pm 0.15\text{ m}^2\text{ g}^{-1}$.^[43] A graphical representation of the SSAs from BET and EDLC is provided in Figure S5, Supporting Information. Regardless of the surface area measurement technique, the porosity-gradient electrodes show higher SSA than their macrovoid counterparts, which we posit plays a significant role on kinetically limited RFB systems.

2.3. Evaluation of Electrodes in Various Flow-Cell Configurations

We now compare the fluid dynamic and electrochemical performance of the porosity-gradient electrode to that of the macrovoid-containing electrode. For electrode evaluation, we employ several cell configurations with differing working fluids and electrolytes. The different cell formats are shown in Figure 4a–d, while the three electrode arrangements investigated are shown in Figure 4e. Specifically, the three electrodes consist of two orientations of the porosity-gradient materials and one arrangement of the macrovoid material. As a reminder, we refer to the case where the porosity increases from the flow field to the membrane as G16_PLM, where PLM stands for “porous layer towards the

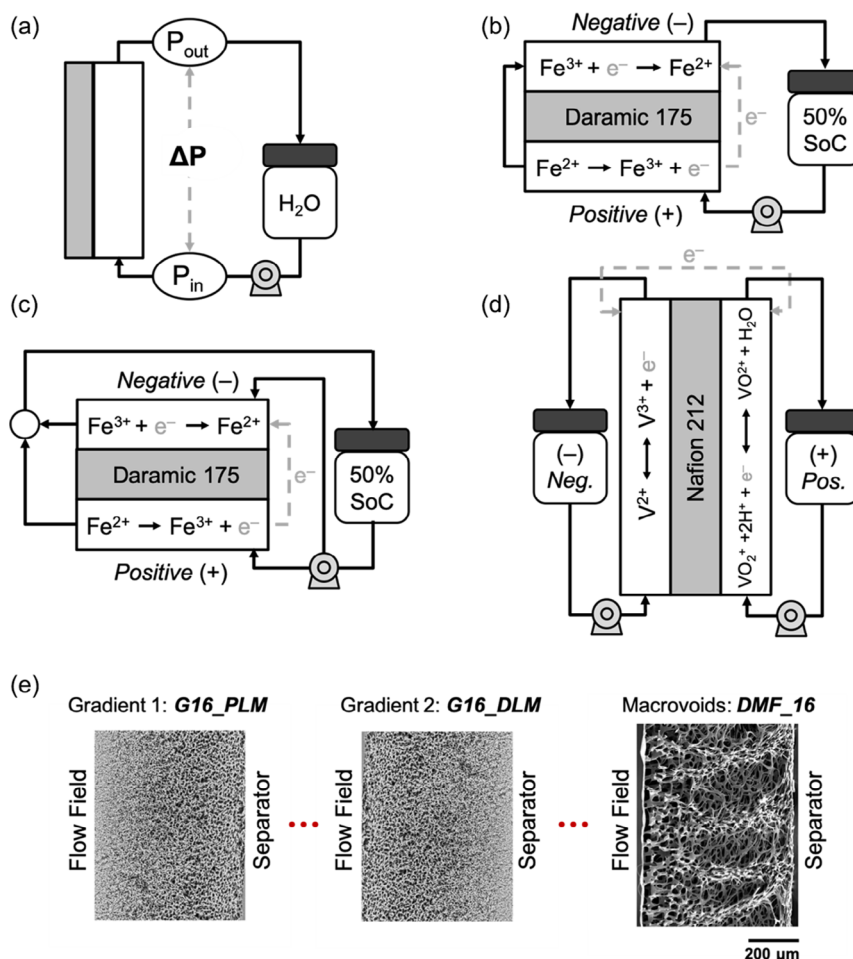


Figure 4. Experimental configurations and orientation of the electrode porosity gradient in the reactor. a) Configuration to estimate the pressure drop, and therefore permeability, of the electrodes. Reactor configurations to perform b) iron chloride single-electrolyte polarization and impedance, c) iron chloride symmetric cell limiting current, and d) full-cell vanadium redox flow battery (VRFB) evaluation. e) Electrodes investigated in this study and their orientation with respect to the flow field and separator, where G16_PLM refers to the more PL facing the membrane, G16_DLM refers to the denser layer facing the membrane, and DMF_16 refers to the macrovoid-containing electrode.

membrane,” and we refer to the case where the porosity decreases from the flow field to the membrane as G16_DLM, where DLM stands for “dense layer towards the membrane.”

2.3.1. Assessing Electrode Permeabilities

We first examine the fluid dynamic performance of the set. **Figure 5a** shows representative pressure drop measurements as a function of linear velocity of the working fluid, here water, through the electrode. To account for differences in electrode thicknesses, we calculate a superficial electrolyte velocity, v (m s^{-1}), using Equation (1)

$$v = \frac{Q}{N t_e w_e} \quad (1)$$

where Q is the volumetric flow rate ($\text{m}^3 \text{s}^{-1}$), N is the number of inlet channels (-), t_e is the compressed electrode thickness (m), and w_e is the electrode width (m). While prior reports elect to

account for electrode porosity to describe electrolyte velocity as an interstitial velocity through the pores,^[73,74] we choose not to do so here due to the complexity of the porosity profiles and spatial variation of the porosities in the present study, rendering interpretation of the interstitial velocity cumbersome.^[12,75] From Figure 5a, it is clear that regardless of the direction of the porosity-gradient material, the permeability is lower than that of the DMF_16. Interestingly, both the G16_PLM and G16_DLM exhibit nearly identical pressure drop despite having opposite porosity profiles. To further investigate the difference in permeabilities of the electrode set, we fit the data to a 1D Darcy–Forchheimer expression relating the pressure drop to the bulk-averaged permeability, κ , Equation (2)

$$\frac{-dP}{dx} = \frac{\mu v}{\kappa} + \beta \rho v^2 \quad (2)$$

where P is the pressure (Pa), x is the position coordinate (m), μ is the dynamic viscosity (Pa s), β is the Forchheimer coefficient

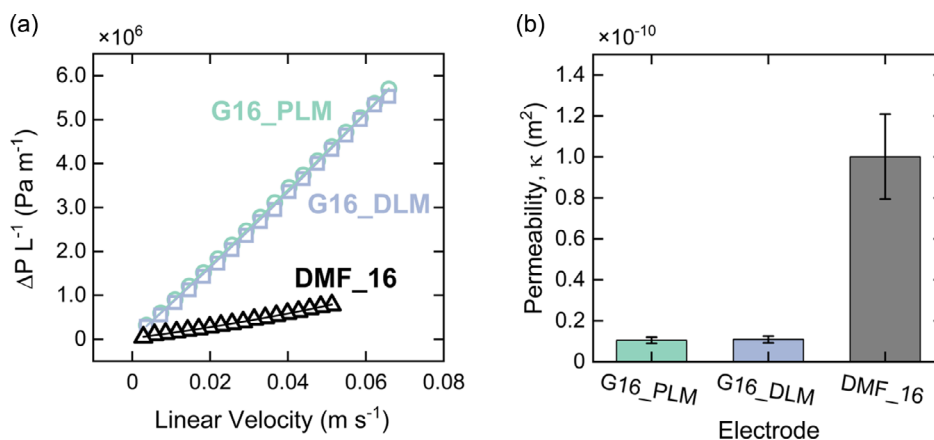


Figure 5. Pressure drop measurements for two directions of the porosity-gradient and macrovoid electrode. a) Representative pressure drop through the electrode as a function of linear velocity. b) Permeability extracted using the Darcy–Forchheimer equation (Equation (2)). Interdigitated flow fields (IDFFs) were used with DI water as the working fluid. All trials were performed in triplicate ($N = 3$).

(m^{-1}), which accounts for inertial effects in the fluid flow, and ρ is the fluid density ($kg m^{-3}$). A table summarizing the extracted effective permeabilities and Forchheimer coefficients are provided in Table S3, Supporting Information. Using this fit, we determine the effective permeability to be $(1.05 \pm 0.15) \times 10^{-11}$, $(1.09 \pm 0.17) \times 10^{-11}$, and $(1.00 \pm 0.21) \times 10^{-10} m^2$ for the G16_PLM, G16_DLM, and DMF_16, respectively (Figure 5b). We note that the results for the DMF_16 are in consonance with our previous work on NIPS electrodes, which displayed permeabilities $O(10^{-10}–10^{-11} m^2)$.^[43] Importantly, while the permeabilities of the porosity-gradient materials are an order of magnitude lower than that of the macrovoid material, they are still within reasonable values for practical operation; for reference, fibrous electrodes used in RFBs exhibit permeabilities spanning $O(10^{-10}–10^{-12} m^2)$.^[12,76] The tradeoff between permeability and ECSA is illustrated in Figure S6, Supporting Information, which further contextualizes the values reported in this study to those obtained from our studies of NIPS electrode materials^[43] and commercially available fibrous electrodes.^[12] The interdigitated flow fields (IDFFs) used in this study lead to lower pressure drops and different flow patterns than other configurations;^[12,77] we leave the investigation of pairing porosity-gradient electrodes with alternative flow-field configurations to future studies.

2.3.2. Electrochemical Evaluation in Iron Chloride Single-Electrolyte Flow Cell

Next, we evaluate the electrochemical performance of the electrodes using a single-electrolyte flow-cell configuration. We measure cell polarization to determine the total resistance and electrochemical impedance spectroscopy (EIS) to determine the sources and relative magnitudes of the resistive losses. As described in previous reports, in the single-electrolyte configuration (Figure 4b), electrolyte is pumped from a reservoir into the positive electrode where it is oxidized, circulated into the negative electrode where it is reduced, and returned to the same reservoir.^[12,42,75,78] It is thus a convenient approach to evaluating cell performance characteristics as a function of constituent

components and operating conditions while maintaining a 50% state of charge (SoC) and minimizing the complexities of cycling a full cell (i.e., crossover, capacity fade) which can convolute data analysis.^[12,42,78] To focus on kinetic and mass-transport resistances, we approximate Ohmic contributions as the product of the current, i , and the high-frequency intercept of the Nyquist plots from EIS, R_{Ω} (vide infra), and subtract the product from the polarization curves. The iR_{Ω} -corrected polarization curves of the three different electrode arrangements at three different linear velocities of 2, 0.5, and $0.1 cm s^{-1}$ in 0.25 M Fe^{2+} and 0.25 M Fe^{3+} in 2 M HCl are shown in Figure 6a–c. Here, we choose iron chloride as a model redox compound due to its moderately fast kinetics on carbon surfaces and chemical reversibility, which is ideal for reducing activation overpotential to enable interrogation of mass-transfer overpotential; further, the behavior of the redox couple within RFBs is relatively well understood as it has been used in several practical embodiments of the technology (e.g., Fe–Cr RFB, hybrid all–Fe RFB).^[74,79] At the highest flow rate of $2 cm s^{-1}$, the G16_PLM and G16_DLM electrodes show identical polarization behavior, both outperforming the DMF_16 electrode. The insensitivity of cell performance to the direction of the porosity gradient is hypothesized to be a consequence of the higher linear velocity combined with the IDFF, which directs fluid velocity components in at least two directions,^[12] and may enable a more uniform velocity profile independent of porosity gradients. We posit that the lower permeability porosity-gradient materials outperform the higher permeability DMF_16 as permeability tends to be inversely related to mass transfer.^[27] We have previously shown that PSD and cell performance tend to also be inversely related in both NIPS materials^[43] and carbon papers,^[12] which we attribute to higher local electrolyte velocities and shorter diffusion lengths within smaller pores, though we acknowledge that additional features of the pore network will also affect fluid dynamics and reactive transport. At an intermediate flow rate of $0.5 cm s^{-1}$, the G16_DLM exhibits the lowest resistances, followed by G16_PLM, and then DMF_16. At the lowest flow rate used in this study, $0.1 cm s^{-1}$, G16_DLM again outperforms the DMF_16 and G16_PLM. We rationalize that for the G16_PLM, performance rapidly decreases with decreasing flow

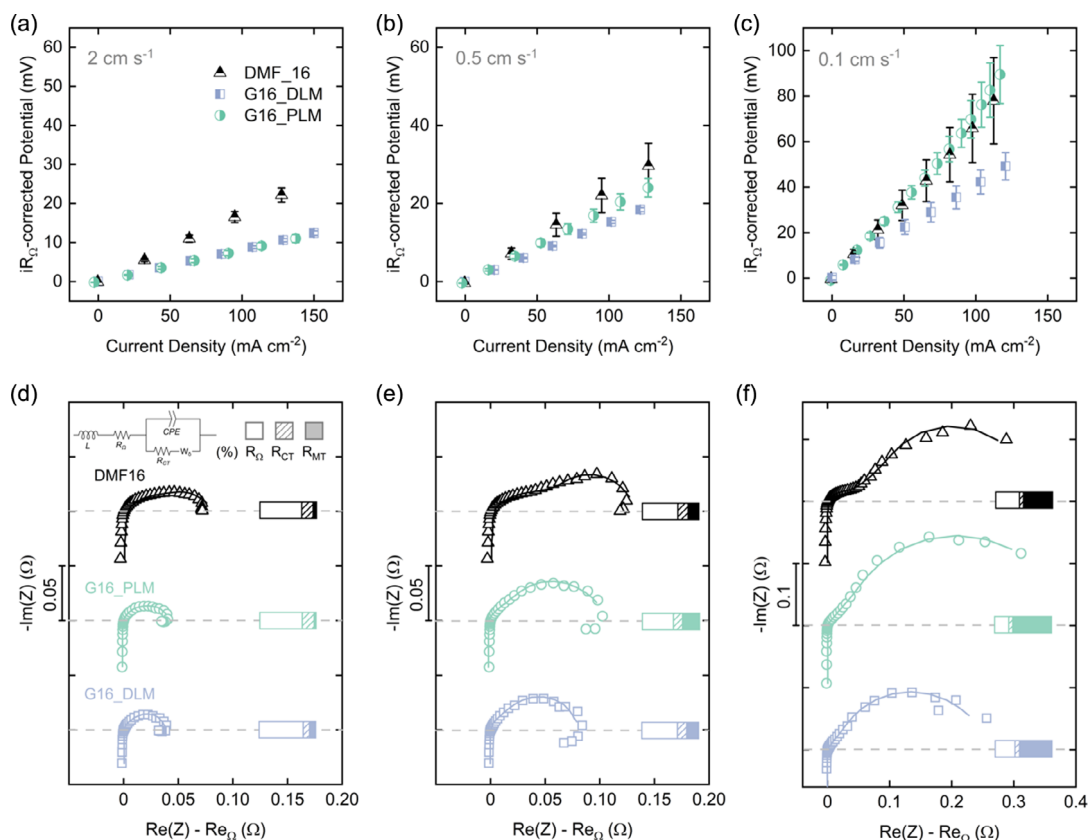


Figure 6. Electrochemical performance of electrodes in iron chloride in the single-electrolyte configuration. The electrolyte solution was 0.25 M Fe^{2+} and 0.25 M Fe^{3+} in 2 M HCl supporting electrolyte. A Daramic 175 membrane was used, along with IDFF at a $\approx 20\%$ compression. Polarization response of electrodes in iron chloride at a) 2, b) 0.5, and c) 0.1 cm s^{-1} linear velocity for the DMF_16, G16_PLM, and G16_DLM electrodes, respectively. Representative Ohmically corrected Nyquist plots from electrochemical impedance spectroscopy (EIS) and breakdown of resistances are shown at linear velocities of d) 2, e) 0.5, and f) 0.1 cm s^{-1} ; experimental data points (symbols) are fit to the modified Randles equivalent circuit model shown in the inset of (d). The bars show the breakdown in the contribution of Ohmic, charger transfer, and mass-transport resistances to overall cell resistance. All trials for each sample were performed in duplicate ($N = 2$).

rate because of reduced transport rates to the electrode surface in the most active zone of the electrode near the membrane. This effect is alleviated at higher flow rates because of thinner boundary layers. These polarization results show the importance of electrolyte flow rate on the relative performance of the electrodes.

We further analyze the breakdown of resistances by fitting Nyquist plots obtained from EIS measurements, conducted about the operating circuit potential, at different electrolyte flow rates to a modified Randles equivalent circuit model (ECM) with a constant phase element (CPE) and bounded Warburg diffusion, shown in Figure 6d–f. In this circuit, L corresponds to inductance from the leads used to connect to the flow cell in the potentiostat, R_{Ω} corresponds to the Ohmic resistance, CPE corresponds to the EDLC, R_{CT} corresponds to the charge-transfer resistance, and R_{MT} , extracted from the Warburg element for convective diffusion, W_{δ} , corresponds to the mass-transfer resistance. We note that an ECM is a useful technique to approximate the cell response as a collection of discrete circuit elements representing known physical processes;^[80,81] however, this approach is not grounded in a first-principles physical basis, and multiple ECMs could be used to adequately fit the data with alternate physical interpretations.^[82,83] Thus, the fits in the present work are intended to

semiquantitatively capture the resistance breakdown across the three porosity profiles as a function of superficial velocity. We acknowledge the presence of low-frequency loops crossing the $-\text{Im}(Z)$ axis at 0.5 and 2 cm s^{-1} flow rates for the G16_PLM and G16_DLM. Similar inductive features observed in PEMFCs have been attributed to side reactions with intermediate species, water transport in the system, or transient catalyst layer proton conductivity.^[84–86] In the present work, we elect not to fit the low inductance loop, although future work should focus on determining the mechanisms leading to the anomalous behavior through physics-based modeling.^[87,88] R_{Ω} for the three electrodes are all comparable, yielding values of $\approx 0.15 \pm 0.03$, 0.28 ± 0.20 , and $0.24 \pm 0.01 \Omega$ (0.39 ± 0.07 , 0.72 ± 0.50 , and $0.62 \pm 0.04 \Omega \text{ cm}^2$) for the G16_PLM, G16_DLM, and DMF_16, respectively, although the measured resistances are only partly due to the effective conductivity resulting from the electrode matrix, and may vary for individual cell builds or lab-specific cell designs.^[9] Corroborating the polarization results, the Nyquist plots evince the same shift in performance trend of the electrodes with flow rate. Initially, at 2 cm s^{-1} , the G16_PLM and G16_DLM show nearly identical spectra, while the DMF_16 shows overall larger resistance. At 0.5 cm s^{-1} , the resistance gap between G16_PLM

and DMF₁₆ becomes closer, whereby G16_DLM has clearly lower kinetic and mass-transport resistance. Finally, at 0.1 cm s⁻¹, G16_PLM has a slightly higher resistance than DMF₁₆, and G16_DLM is the best performer. Again, these results are consistent with those observed in the *i*R_Ω-corrected polarization curves. A breakdown of *R*_{CT} and *R*_{MT} from the ECM fittings for the electrodes with varying flow rate is shown in Figure S7, Supporting Information, and a summary of the parameters extracted from the ECM fit as well as fit quality is provided in Table S4, Supporting Information. For all electrodes, the *R*_{CT} does not vary by more than a factor of two irrespective of flow rate, in consonance with expectations that reaction rate should be independent of flow rate. However, we observe a significant increase in *R*_{MT} with decreasing flow rate and G16_PLM appears the most sensitive to flow rate; semi-quantitatively, the ratio between *R*_{MT} at 0.1 cm s⁻¹ to *R*_{MT} at 2 cm s⁻¹ is ≈67×, 15×, and 12× for G16_PLM, DMF₁₆, and G16_DLM, respectively. This strong dependence on flow rate for the G16_PLM may ultimately be responsible for the relatively higher resistances at low flow rate. Limiting current measurements were also performed to further investigate mass transfer of these electrodes and compare them to fibrous electrodes in the literature (see Section S9, Supporting Information).

2.3.3. Electrochemical Evaluation in a VRFB Full Cell

We next assess the performance of the porosity-gradient electrodes in VRFB full cells, arguably the state-of-the-art RFB chemistry.^[89] In contrast to the moderately fast reaction kinetics of the aqueous iron chloride couple on carbon surfaces, the vanadium redox reaction kinetics are generally observed to be sluggish on carbon surfaces.^[90] We first compare the performance of G16_PLM, G16_DLM, and DMF₁₆ *via* a rate study where the flow cell is galvanostatically cycled at five different current densities of increasing magnitude (100, 150, 200, 250, and 300 mA cm⁻²) and then returned to the initial current density (100 mA cm⁻²), to evaluate performance recovery after high-rate cycling, with five charge/discharge cycles per current density. The reported efficiency values correspond to the steady-state efficiencies reached during the last cycles of each current density step. An electrolyte composition of 1.0 M vanadium in 3.0 M H₂SO₄ was chosen to demonstrate the practical application of the porosity-gradient electrodes in VRFBs. Experiments were performed at a flow rate of 2 cm s⁻¹ to identify the upper bound of cell performance in the operating conditions used in this study. Charge/discharge curves and corresponding efficiencies for the flow cells with the three different electrode arrangements are shown in Figure 7. Under this set of flow rates, flow fields, and electrolyte composition, the G16_PLM demonstrated the highest overall energy efficiency at all current densities examined. Furthermore, porosity-gradient electrodes outperformed their macrovoid counterpart by a significant margin (i.e., the performance of the cells with G16_PLM and G16_DLM is superior to the performance of the cell with DMF₁₆). Across all cycles, the average Coulombic efficiencies of G16_PLM, G16_DLM, and DMF₁₆ were comparable, achieving ≈97.9 ± 0.6%, 98.0 ± 0.7%, and 97.6 ± 1.1%, respectively. However, the G16_PLM and G16_DLM showed higher energy efficiencies at all current densities than the DMF₁₆. Specifically, at current densities of 100, 200, and 300 mA cm⁻², the G16_PLM achieved

energy efficiencies of 89.3 ± 0.1%, 82.8 ± 0.1%, and 76.1 ± 0.7%, as compared to that of the G16_DLM (88.3 ± 0.2%, 79.8 ± 0.1%, and 72.5 ± 1.0%) and DMF₁₆ (79.6 ± 0.3%, 67.9 ± 0.1%, and 54.4 ± 5.2%), respectively. Overall, the energy efficiency of the G16_PLM is ≈21.7% higher than the DMF₁₆ at the highest current density, 300 mA cm⁻². As evinced in the aforementioned energy efficiencies, while G16_PLM and G16_DLM displayed similar performances, disparities gradually widened with increasing current density, whereby the G16_PLM demonstrated better rate capability by a small margin. Discharge polarization further supports this trend observed in the rate study (Figure S9, Supporting Information). The maximum power densities of the G16_PLM, G16_DLM, and DMF₁₆ were ≈858, 826, and 447 mW cm⁻², respectively. Thus, the porosity-gradient materials attained significantly higher power densities, and the G16_PLM exhibited slightly higher power densities than the G16_DLM. Generally, the higher surface area porosity-gradient materials performed better when compared to the more porous and lower surface area DMF₁₆. The results illustrate that for this cell geometry, electrolyte composition, and electrolyte flow rate, higher porosity facing the membrane leads to a slight advantage at higher current densities. We hypothesize that in the current distribution formed as a result of the sluggish vanadium redox reaction, higher porosity near the membrane combined with lower porosity at the flow field leads to increased local electrolyte velocities near the membrane, enabling greater flux of active species to be replenished as the driving force (i.e., current density) is increased. These findings are in agreement with a recent publication, which suggests that larger pores near the membrane are advantageous.^[28] Interestingly, the results in vanadium differ from the single-electrolyte iron chloride data, highlighting the nuance in guiding the better gradient profiles for unique circumstances. Overall, the porosity-gradient materials are also characterized by higher surface area and lower permeability than the DMF₁₆, which have been shown to lead to improved performance in VRFB full cells.^[42,43] Ultimately, the type of porosity gradient will have a significant impact on which direction of the gradient is definitively better for performance.

Electrodes processed at lower carbonization temperatures may be susceptible to degradation during longer duration cycling. While durational studies are challenging in an academic laboratory, we seek to evaluate the short-term durability of the electrodes. For the rate study, all electrodes appear to retain their performance, all returning to the initial current density of 100 mA cm⁻² with a decrease of ≈1% energy efficiency. The rate studies lasted ≈2.0 days for the G16_PLM and G16_DLM, and ≈1.4 days for the DMF₁₆. The best-performing G16_PLM electrode was subjected to a longer cycling experiment, cycled 206× at 100 mA cm⁻² (≈12.4 days). The efficiencies remained relatively consistent when cycling. An average Coulombic efficiency of ≈97.8 ± 0.4% and voltaic efficiency of ≈89.5 ± 0.9% was achieved, leading to an energy efficiency of 87.6 ± 0.7%, with a ≈2.2% reduction in energy efficiency from cycle 1–206 (Figure 7g). The discharge capacity as a function of cycle number, shown in Figure 7g, starts at ≈72.3% of the theoretical maximum discharge capacity of 26.8 Ah L⁻¹ and decays at a rate of 0.372% per cycle. This fade rate is comparable to the benchmark of 0.442% per cycle from a recent study which contains a summary of capacity fades reported in the open literature.^[91] The discharge capacity decay combined with the relatively steady efficiencies for

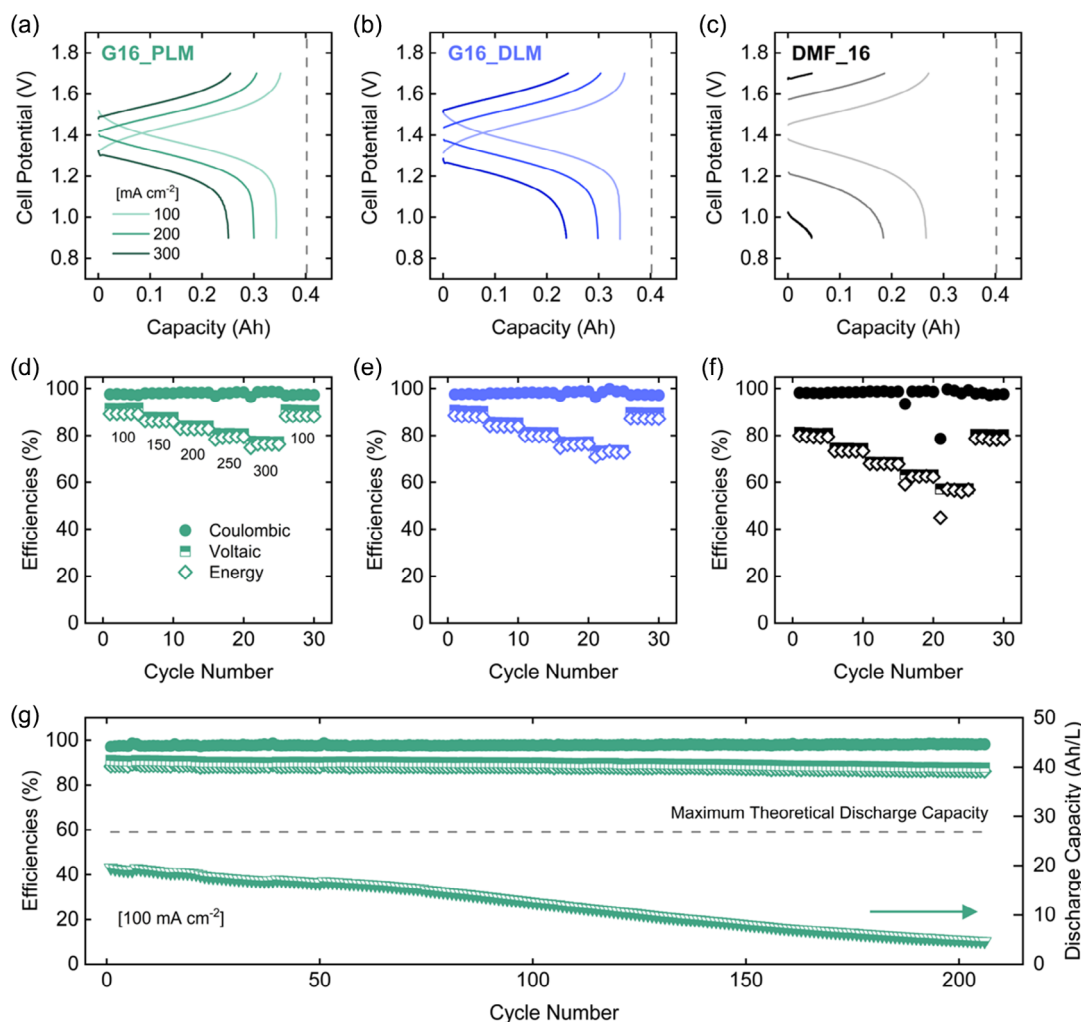


Figure 7. Evaluation of electrodes in 1.0 M vanadium in 3.0 M H_2SO_4 electrolyte for the gradient porosity electrode and the macrovoid-containing electrode at a 2 cm s^{-1} linear velocity. a–c) Galvanostatic cycling curves at current densities of 100, 200, and 300 mA cm^{-2} . The maximum theoretical discharge capacity, 0.402 Ah , is plotted in grey. d–f) Coulombic, voltaic, and energy efficiencies as a function of current densities from 100, 150, 200, 250, and 300 mA cm^{-2} , followed by recovery to 100 mA cm^{-2} . g) Efficiencies and discharge capacity of the G16_PLM over 200 cycles at a current density of 100 mA cm^{-2} , lasting over a ≈ 12.4 day span. The theoretical maximum discharge capacity, determined to be 26.8 Ah L^{-1} for 15 mL of electrolyte and 1.0 m vanadium, is plotted for reference. All trials were performed once ($N = 1$).

the G16_PLM electrode suggests that the fade is largely driven by active species crossover.

We briefly contextualize the results obtained for our porosity-gradient material to a non-exhaustive set of recent studies in the VRFB literature, acknowledging that quantitative comparisons are challenged by differences in operating procedures, choice of cell component materials, and lab-specific flow-cell reactor designs. A graphical comparison of energy efficiencies as a function of current density from these studies is provided in Figure S10, Supporting Information, and a description of the experimental conditions of the studies is summarized in Table S6, Supporting Information. Zhang et al. developed a N, P co-doped/reduced graphene oxide-coated carbonized melamine foam electrode that yielded a 74.14% energy efficiency at a current density of 300 mA cm^{-2} .^[92] Deng et al. synthesized porous lamellar carbon from *Bacillus mycoides* to form an electrode for

VRFBs, achieving a $\approx 73.9\%$ energy efficiency at a current density of 200 mA cm^{-2} .^[93] Park et al. used corn protein-derived particles on carbon felt electrodes to yield an energy efficiency of 68.6% at a rate of 150 mA cm^{-2} .^[94] Overall, the results presented in our work on porosity-gradient materials appear comparable to prior reports.

3. Conclusions

Optimizing the porous carbon electrode microstructure is essential to achieving high energy efficiency and high power density RFBs. Commercial electrode microstructures constrain the available design space of pore networks, necessitating the development of bottom-up engineered electrodes. Furthermore, unlike the macrohomogeneous properties of commercial offerings,

porosity-gradient electrodes may hold promise to effectively balance electrolyte distribution through the electrode while providing ample surface area in reaction-limited regions of the electrode. In this work, we demonstrate a versatile and bottom-up extension to the NIPS method to fabricate porosity-gradient electrode microstructures derived from PAN by adding a buffer layer of DMF prior to the non-solvent phase-separation step. Image analysis reveals the electrodes are characterized by monotonically and exponentially increasing porosity evolving from the bath/polymer interface to the polymer/mold interface, with an average porosity of ≈ 0.5 . Additionally, the electrodes are free of macrovoids on the sub-centimeter scale, in contrast to electrodes synthesized directly using NIPS without the buffer layer. Using the same polymer solution formulation, we compare the porosity-gradient electrode to its macrovoid-containing counterpart. Materials characterization of the porosity-gradient and macrovoid-containing electrodes show that the electrodes share similar crystallinity, vibrational properties, and surface chemistries, though the porosity-gradient electrodes have higher surface areas. We then compare the effect of the direction of the porosity gradient on fluid dynamic and electrochemical performance and benchmark the results to the macrovoid-containing electrode. We find that the porosity-gradient electrodes have an order of magnitude lower permeability than the macrovoid-containing electrode, and that interestingly, the direction of the porosity gradient does not affect the permeability; we attribute this to the use of IDFF, which accommodate flow in multiple directions for improved electrolyte distribution. In iron chloride single-electrolyte electrochemical measurements, we find the performance trends of the electrodes to be flow-rate dependent. Specifically, while the porosity-gradient electrodes both equally outperform the macrovoid counterpart at high flow rate, the G16_PLM performs relatively worse at an intermediate flow rate and shows the highest resistances of the set at the lowest flow rate. Subsequently, we evaluate the practical application of these electrodes in a full-cell VRFB, determining that the porosity-gradient electrodes exhibit significantly greater energy efficiency and power density as compared to the macrovoid-containing electrode, and are in good standing when contextualized to bottom-up engineered electrode efforts in the VRFB literature. Looking forward, this method offers a new platform which may be used to further explore porosity profiles of varying shape (e.g., linear, step-wise, quadratic) and amplitude (i.e., upper and lower bounds). The proven microstructural diversity of phase-separated electrodes provides new opportunities for the development of porous materials with tailored property sets for RFBs-containing electrolytes with distinct electrochemical and rheological characteristics. Further investigations in synthetic capabilities may enable articulation of the flow-rate-dependent mass-transport behavior observed in the present work to fully harness the potential of porosity-gradient electrodes in RFBs and electrochemical systems more broadly.

4. Experimental Section

Electrode Synthesis: Membrane Formation and Phase Separation: PAN (average molecular weight $\approx 150\,000$, Sigma Aldrich), PVP (average molecular weight $\approx 1\,300\,000$, Alfa Aesar), and DMF (suitable for high-performance liquid chromatography (HPLC), $\geq 99\%$, Sigma Aldrich) were

dissolved through continuous mixing with a metal spatula and heating at $70\text{ }^\circ\text{C}$ in a drying oven (Heratherm OMH60, ThermoScientific) in a 100 mL Pyrex Media Bottle (VWR) for a total of ≈ 1 h. Afterwards, the media bottle was placed on a roller mixer (SCI-T6-S, Scilogex) at a setting of ≈ 40 rpm at room temperature. The viscous mixture was subsequently cast into five separate $7\text{ cm} \times 5\text{ cm} \times 0.11\text{ cm}$ ($L \times W \times H$) aluminum molds arranged on a $12'' \times 8'' \times 1/8''$ ($L \times W \times H$) glass substrate (McMaster-Carr). A glass microscope slide (McMaster-Carr, 1149T11) was used to evenly distribute the solution into the aluminum molds. To create scaffolds with macrovoid structures, the casted molds were rested in ambient conditions for ≈ 15 min to enable VIPS which results in removal of the dense top layer;^[43] then, the entire assembly was submerged into a 1.25 gallon capacity $17\ 1/4'' \times 10\ 3/4'' \times 2\ 3/8''$ ($L \times W \times H$) glass pan (McMaster-Carr) filled with 3 L of deionized (DI) water (Milli-Q Millipore, $18.2\ \text{M}\Omega\ \text{cm}$) to initiate the NIPS process, where the PVP and DMF leached into the DI water bath, resulting in a porous PAN microstructure. For the macrovoid-free porosity-gradient structures, the VIPS step was omitted, and instead, after casting, the entire assembly was submerged into a separate glass pan filled with 1 L DMF for ≈ 5 s, and then immediately transferred into the 3 L DI water bath to complete the phase-separation process. Exposing the casted molds to DMF created a buffer between the non-solvent and the solution, reducing instantaneous demixing, and preventing the formation of macrovoids (vide supra for a more detailed discussion of the hypothesized mechanism). This resulted in a porosity profile that naturally increases when going from the bath/polymer interface to the polymer/mold substrate interface. The membranes were left in the water bath overnight to allow for the phase-separation process to equilibrate.

Electrode Synthesis: Drying, Thermal Stabilization, and Carbonization of Membranes: After the phase-separation process, the membranes were removed from the molds and soaked in a 1200 mL crystallizing dish (VWR) with boiling DI water to drive additional PVP and DMF removal in a vented fume hood. The boiling water was replaced periodically until the water appeared completely clear ($\approx 3\text{--}4$ rinses over a 1 h span). Then, the membranes were dried between Scott C-Fold paper towels (VWR), placed between two $1/16''$ thick polytetrafluoroethylene (PTFE) sheets (McMaster-Carr) cut to $10'' \times 8''$ ($L \times W$), sandwiched between $10'' \times 8'' \times 1/8''$ glass plates (McMaster-Carr) with a total applied weight of ≈ 372 g, and dried under vacuum (≈ 2 Torr) using a Welch 2032 vacuum pump (Cole-Parmer) in a vacuum oven (Fisher Scientific) at $80\text{ }^\circ\text{C}$ for ≥ 4 h. The dried membranes were then removed from between the PTFE sheets and placed between two sheets of alumina paper (ZIRCAR Ceramics Inc.), compressed by a graphite block (isomolded graphite plate, fuel cell store) machined into a $12 \times 14 \times 0.318\text{ cm}$ ($L \times W \times H$) prism weighing ≈ 50 g, and thermally stabilized in a muffle furnace (Barnstead Thermolyne Type 47900) at $270\text{ }^\circ\text{C}$ for 1 h with a ramp rate of $2\text{ }^\circ\text{C}$, followed by a cooldown to room temperature without intervention. The thermally stabilized membranes were then placed in between two graphite blocks (McMaster-Carr, 9121K67) milled down to a thickness of 0.318 cm with a total applied weight of 124 g on the thermally stabilized membranes, and carbonized in a tube furnace (GHA 12/300 Furnace, Carbolite) under flowing nitrogen (Airgas, 99.999%) at a $\approx 2\text{ L min}^{-1}$ flow rate using the following sequence: ramped from room temperature to $850\text{ }^\circ\text{C}$ at a rate of $5\text{ }^\circ\text{C min}^{-1}$, held for 40 min, ramped to $1050\text{ }^\circ\text{C}$ at a rate of $5\text{ }^\circ\text{C min}^{-1}$, held for 40 min, and cooled down to room temperature without intervention. The synthesized electrodes were stored in plastic containers under ambient conditions.

Ex Situ Characterization: SEM was performed on a Phenom ProX desktop SEM (Nanoscience Instruments Inc.). A 15 kV electron energy, ≈ 6.5 mm working distance, and $\approx 370\times$ magnification were used to collect the images. Three porosity-gradient electrode cross sections from different samples were imaged. To determine the electrode surface chemistry, XPS was performed on a Thermo Scientific K- α System equipped with a monochromatic small-spot X-Ray source and a 180° double-focusing hemispherical analyzer with a 128-channel detector ($N = 1$ for each electrode type); the conditions are described in a previous report.^[42] The molecular vibrational modes of the electrodes were examined through Raman spectroscopy using a 300 R confocal Raman microscope ($N = 1$ for each electrode

type) using a UHTS300S_Green_NIR at a wavelength of $\lambda = 532.306$ nm. XRD spectra ($N = 1$ for each electrode type) were collected using a PANalytical X'Pert Pro MPD (Malvern Panalytical, UK) in the Open Eulerian Cradle configuration. A fixed aperture of $1/4^\circ$ with a $1/2^\circ$ Soller slit was used during collection. The X-Ray source was a Cu anode with a $K\text{-}\alpha$ wavelength of 1.54060 Å. BET surface area of electrode materials were measured using Ar-gas physisorption with a TriStar II PLUS instrument from Micromeritics. The different electrodes were cut into square of $\approx 2 \times 2$ mm and dried at 80°C under vacuum for 24 h prior to analysis. A sample mass of roughly 100 mg was used for each BET experiment (due to imperfect cutting of the samples, the masses spanned 95–115 mg). Helium was used to titrate the volume of voids in the measuring vessel (volume not occupied by the sample). After helium evacuation and purging the measuring vessel with argon, the partial pressure of argon was slowly ramped from $p/p^0 = 0$ until 0.98 after which the reverse process was performed. The quantity of adsorbed gas was used to estimate the total surface area of the porous electrodes using the BET theory. Analysis of PSDs was performed through MIP using an AutoPore IV 9500 following the conditions of a previous report.^[43] Pore diameters were estimated assuming a cylindrical shape and mercury-carbon contact angles of 130° (advancing and receding). The porosity of bulk electrodes were estimated by registering the mass of the material before and after full imbibition with mercury, assuming complete pore filling. The electrode samples were first cut into small square pieces of $\approx 1 \times 1$ mm before loading in the penetrometer to statistically reduce possible ink-bottle artifacts (i.e., pores that are not connected to the surface of the sample through larger pores) coming from the presence of macrovoids to get a better approximation of the “true” PSD of measured samples.^[95,96]

Image Analysis Procedure: SEM images were binarized and analyzed using Fiji version 2.3.0/1.53q.^[97] Images thresholding was performed by setting pixels from 140 to 255 as part of the solid matrix, and anything below 140 as the pore space. A density profile spanning the cross section was extracted and fit to an exponential with an offset function in Fiji, yielding the profile for the solid matrix based on the positionally averaged gray values, $GV(z)$. To obtain the porosity, ϵ , the solid matrix profile was inverted using the equation $\epsilon(z) = 1 - \frac{GV(z)}{255}$. The values for three cross sections of distinct samples were averaged to determine the porosity profile.

Flow Cell Measurement Setup: An in-house built redox flow cell with a 2.55 cm^2 (1.5×1.7 cm) geometric active area was used in all flow battery experiments, along with IDFFs milled from Tokai G347B resin-impregnated graphite plates of 3.18 mm thickness (Tokai Carbon Co.) with four inlet channels and three outlet channels; engineering drawings are provided in a previous open-access report.^[73] The $1 \times$ electrode was used on each side (i.e., one positive electrode and one negative electrode without stacking). PTFE gaskets (McMaster-Carr) cut with 1.5×1.7 cm openings were selected to have a thickness $\approx 80\%$ of the nominal electrode thickness, leading to a $\approx 20\%$ for all experiments. Nominal electrode thicknesses were measured using a dial thickness gauge (500-195-30, Mitutoyo); the thicknesses for the porosity-gradient and macrovoid-containing electrodes were measured to be 468.3 ± 21.7 and $575.5 \pm 11.2\ \mu\text{m}$, respectively. Flow rates were maintained with a MasterFlex pump (Cole-Parmer) and circulated using LS/14 Norprene tubing (Cole-Parmer).

Flow Cell Measurement Setup: Permeability Measurements: Measurements were performed in the 2.55 cm^2 flow cell with an IDFF sandwiched with an impermeable resin-impregnated graphite backing plate and DI water as the working fluid. The pressure drop was determined by taking the difference between the pressure at the inlet and outlet of the cell using digital gauges (XP2i Digital Pressure Gauge, AMETEK STC). The flow rate was increased from 5 to 90 mL min^{-1} , and then decreased back to 5 mL min^{-1} at increments of 5 mL min^{-1} . Each flow rate was held for 20 s to ensure a stable reading was obtained. All trials for each electrode type were performed in triplicate ($N = 3$). The experimentally measured data was fit to the Darcy-Forchheimer equation in MATLAB 2022a to extract permeability values.

Flow Cell Measurement Setup: Iron Chloride Flow Cell Experiments: Iron (II) chloride tetrahydrate ($\text{FeCl}_2 \cdot 4\text{H}_2\text{O}$, 98%, Sigma Aldrich), iron (III) chloride hexahydrate ($\text{FeCl}_3 \cdot 6\text{H}_2\text{O}$, 97%, Sigma Aldrich), and hydrochloric acid (HCl, 37%, balance of water, Sigma Aldrich) were dissolved in DI water and used as received with no further purification prior to experiments. For the single electrolyte experiments, the electrolyte was 15 mL of 0.25 M Fe^{2+} and 0.25 M Fe^{3+} for a total concentration of 0.5 M at 50% SoC in 2 M HCl. For the limiting current experiments, the electrolyte was 50 mL of 0.05 M Fe^{2+} and 0.75 M Fe^{3+} for a total concentration of 0.8 M in 2 M HCl electrolyte; the concentration of Fe^{2+} was intentionally lower to ensure that limiting currents were determined by the oxidation of Fe^{2+} .^[73] For both limiting current and single-electrolyte experiments, the order of experiments was from high to low flow rates. Prior to the single electrolyte experiments, the cell was preconditioned by applying a 25 mV bias for 30 min at a 3 cm s^{-1} flow rate to allow the cell to equilibrate and wet.^[75] Daramic 175 (175 μm thick, Daramic) microporous separator was used as received. The volumetric flow rate was adjusted to match superficial electrode velocities. For the single-electrolyte polarization measurements, a constant voltage was applied beginning at 0 V and increasing stepwise by 25 mV and up to 0.4 V, with a 1 min hold at each potential. The current from the last 50% of each potential hold was averaged and reported to ensure the cell had reached steady state. For the EIS measurements, a 10 mV potential amplitude around open-circuit voltage was used across a range of 200 Hz to 10 mHz with six points per decade in logarithmic spacing and two average measures per frequency. For the limiting current experiments, a constant voltage was applied beginning at 0 V and increasing stepwise by 25 mV until a limiting current was reached (usually up to 0.6 V). A 30 s hold was employed at each potential, and the last half of the recorded current at each potential hold was averaged to ensure the cell was near steady state. Measurements for the single-electrolyte polarization and EIS were conducted using a Bio-Logic VSP potentiostat (Bio-Logic), whereas measurements for the limiting current experiments were conducted with an Arbin battery tester (FBTS-8).

Flow Cell Measurement Setup: VRFB Full-Cell Experiments: For all experiments, the starting solution consisted of 1 M vanadium (IV) sulfate oxide hydrate (99.9%, Fisher Scientific) and 3 M sulfuric acid (H_2SO_4 , 95.0–98.0%, Sigma Aldrich) dissolved in DI water. A Nafion 212 membrane (50.8 μm nominal thickness, Fuel Cell Store) was pretreated by soaking in 3 M H_2SO_4 for ≥ 24 h prior to use. The procedure to procure 50% SoC electrolyte is detailed elsewhere.^[43,98,99] Positive electrolyte of 15 mL and negative electrolyte of 15 mL were used in VRFB full-cell experiments. To determine the discharge polarization of the cells, the discharge current was increased at intervals of 20 mA cm^{-2} followed by alternating charge at fixed 100 mA cm^{-2} to return to 50% SoC, determined Coulombically. For the rate study, the current density was increased from 100, 150, 200, 250, and 300 mA cm^{-2} , followed by a return to 100 mA cm^{-2} . Potential limits were set at 0.9 V while discharging and 1.7 V during charging to limit side reactions. Measurements were conducted with an Arbin battery tester (FBTS-8).

Supporting Information

Supporting Information is available from the Wiley Online Library or from the author.

Acknowledgements

The authors acknowledge the support by MIT's Center for Materials Science and Engineering's shared experimental facilities, and the support in part by the MRSEC Program of the National Science Foundation under award no. DMR1419807. Research by C.T.W. and F.R.B. was supported by the Joint Center for Energy Storage Research (JCESR), an Energy Innovation Hub funded by the U.S. Department of Energy, Office of Science, Basic Energy Sciences. C.T.W. acknowledges the graduate fellowship through the National Science Foundation Graduate Research Fellowship Program under grant no. 1745302. Any opinions, findings, and conclusions or recommendations expressed in this material are those of the authors and do

not necessarily reflect the views of the National Science Foundation. A.F.C. gratefully acknowledges the Dutch Research Council (NWO) for financial support through the Talent Research Program Veni (17324).

Conflict of Interest

The authors declare no conflict of interest.

Author Contributions

C.T.-C.W.: Conceptualization, Methodology, Software, Validation, Formal Analysis, Investigation, Data Curation, Writing—Original Draft, Writing—Review & Editing, Visualization. R.R.J.: Conceptualization, Methodology, Investigation, Writing—Original Draft, Writing—Review & Editing. Y.-M.C.: Funding Acquisition. A.F.-C.: Conceptualization, Funding Acquisition, Writing—Original Draft, Writing—Review & Editing. F.R.B.: Conceptualization, Funding Acquisition, Writing—Original Draft, Writing—Review & Editing, Project administration.

Data Availability Statement

The data that support the findings of this study are available from the corresponding author upon reasonable request.

Keywords

mass transport, non-solvent-induced phase separation, porosity-gradient microstructures, porous carbon electrodes, redox flow batteries

Received: February 15, 2023

Revised: April 17, 2023

Published online: June 6, 2023

- [1] S. Chu, Y. Cui, N. Liu, *Nat. Mater.* **2017**, *16*, 16.
- [2] J. M. Carrasco, L. G. Franquelo, J. T. Bialasiewicz, E. Galvan, R. C. PortilloGuisado, M. A. M. Prats, J. I. Leon, N. Moreno-Alfonso, *IEEE Trans. Industr. Electron.* **2006**, *53*, 1002.
- [3] Z. Yang, J. Zhang, M. C. W. Kintner-Meyer, X. Lu, D. Choi, J. P. Lemmon, J. Liu, *Chem. Rev.* **2011**, *111*, 3577.
- [4] L. F. Arenas, C. Ponce de León, F. C. Walsh, *J. Energy Storage* **2017**, *11*, 119.
- [5] L. F. Arenas, C. Ponce de León, F. C. Walsh, *Curr. Opin. Electrochem.* **2019**, *16*, 117.
- [6] R. M. Darling, K. G. Gallagher, J. A. Kowalski, S. Ha, F. R. Brushett, *Energy Environ. Sci.* **2014**, *7*, 3459.
- [7] C. Sun, H. Zhang, *ChemSusChem* **2022**, *15*, 202101798.
- [8] M. Li, Z. Rhodes, J. R. Cabrera-Pardo, S. D. Minteer, *Sustain. Energy Fuels* **2020**, *4*, 4370.
- [9] D. S. Aaron, Q. Liu, Z. Tang, G. M. Grim, A. B. Papandrew, A. Turhan, T. A. Zawodzinski, M. M. Mench, *J. Power Sources* **2012**, *206*, 450.
- [10] M. Guarnieri, A. Trovò, A. D'Anzi, P. Alotto, *Appl. Energy* **2018**, *230*, 1425.
- [11] A. Z. Weber, M. M. Mench, J. P. Meyers, P. N. Ross, J. T. Gostick, Q. Liu, *J. Appl. Electrochem.* **2011**, *41*, 1137.
- [12] A. Forner-Cuenca, E. E. Penn, A. M. Oliveira, F. R. Brushett, *J. Electrochem. Soc.* **2019**, *166*, A2230.
- [13] B. Sun, M. Skyllas-Kazacos, *Electrochim. Acta* **1992**, *37*, 1253.
- [14] K. V. Greco, A. Forner-Cuenca, A. Mularczyk, J. Eller, F. R. Brushett, *ACS Appl. Mater. Interfaces* **2018**, *10*, 44430.
- [15] K. V. Greco, J. K. Bonesteel, N. Chanut, C. Tai-Chieh Wan, Y.-M. Chiang, F. R. Brushett, *ACS Appl. Energy Mater.* **2021**, *4*, 13516.
- [16] Y. Men, T. Sun, *Int. J. Electrochem. Sci.* **2012**, *7*, 7.
- [17] S. M. Taylor, A. Pătru, D. Streich, M. El Kazzi, E. Fabbri, T. J. Schmidt, *Carbon* **2016**, *109*, 472.
- [18] X. Wu, H. Xu, P. Xu, Y. Shen, L. Lu, J. Shi, J. Fu, H. Zhao, *J. Power Sources* **2014**, *263*, 104.
- [19] M. H. Chakrabarti, N. P. Brandon, S. A. Hajimolana, F. Tariq, V. Yufit, M. A. Hashim, M. A. Hussain, C. T. J. Low, P. V. Aravind, *J. Power Sources* **2014**, *253*, 150.
- [20] K. J. Kim, M.-S. Park, Y.-J. Kim, J. H. Kim, S. X. Dou, M. Skyllas-Kazacos, *J. Mater. Chem. A* **2015**, *3*, 16913.
- [21] A. Forner-Cuenca, F. R. Brushett, *Curr. Opin. Electrochem.* **2019**, *18*, 113.
- [22] J. Sun, M. Wu, H. Jiang, X. Fan, T. Zhao, *Adv. Appl. Energy* **2021**, *2*, 100016.
- [23] J. Sun, H. R. Jiang, B. W. Zhang, C. Y. H. Chao, T. S. Zhao, *Appl. Energy* **2020**, *259*, 114198.
- [24] J. Sun, H. R. Jiang, M. C. Wu, X. Z. Fan, C. Y. H. Chao, T. S. Zhao, *Appl. Energy* **2020**, *271*, 115235.
- [25] J. Sun, M. C. Wu, X. Z. Fan, Y. H. Wan, C. Y. H. Chao, T. S. Zhao, *Energy Storage Mater.* **2021**, *43*, 30.
- [26] M. D. R. Kok, R. Jervis, D. Brett, P. R. Shearing, J. T. Gostick, *Small* **2018**, *14*, 1703616.
- [27] M. D. R. Kok, R. Jervis, T. G. Tranter, M. A. Sadeghi, D. J. L. Brett, P. R. Shearing, J. T. Gostick, *Chem. Eng. Sci.* **2019**, *196*, 104.
- [28] R. van Gorp, M. van der Heijden, M. Amin Sadeghi, J. Gostick, A. Forner-Cuenca, *Chem. Eng. J.* **2022**, 139947.
- [29] M. van der Heijden, R. van Gorp, M. A. Sadeghi, J. Gostick, A. Forner-Cuenca, *J. Electrochem. Soc.* **2022**, *169*, 040505.
- [30] S. Wan, X. Liang, H. Jiang, J. Sun, N. Djilali, T. Zhao, *Appl. Energy* **2021**, *298*, 117177.
- [31] D. Maggiolo, F. Picano, M. Guarnieri, *Phys. Fluids* **2016**, *28*, 102001.
- [32] V. A. Beck, J. J. Wong, C. F. Jekel, D. A. Tortorelli, S. E. Baker, E. B. Duoss, M. A. Worsley, *J. Power Sources* **2021**, *512*, 230453.
- [33] J. K. Lee, C. Lee, K. F. Fahy, P. J. Kim, J. M. LaManna, E. Baltic, D. L. Jacobson, D. S. Hussey, S. Stiber, A. S. Gago, K. A. Friedrich, A. Bazylak, *Energy Convers. Manage.* **2020**, *226*, 113545.
- [34] V. Ramadesigan, R. N. Methekar, F. Latinwo, R. D. Braatz, V. R. Subramanian, *J. Electrochem. Soc.* **2010**, *157*, A1328.
- [35] M. Balakrishnan, P. Shrestha, N. Ge, C. Lee, K. F. Fahy, R. Zeis, V. P. Schulz, B. D. Hatton, A. Bazylak, *ACS Appl. Energy Mater.* **2020**, *3*, 2695.
- [36] Q. Wu, Y. Lv, L. Lin, X. Zhang, Y. Liu, X. Zhou, *J. Power Sources* **2019**, *410–411*, 152.
- [37] H. R. Jiang, B. W. Zhang, J. Sun, X. Z. Fan, W. Shyy, T. S. Zhao, *J. Power Sources* **2019**, *440*, 227159.
- [38] J. LORETZ, S. V. Puranam, H. E. Vanbenschoten, US10109879B2, **2018**.
- [39] W. Chen, J. Kang, Q. Shu, Y. Zhang, *Energy* **2019**, *180*, 341.
- [40] W. Chen, J. Kang, *Chem. Phys.* **2020**, *529*, 110577.
- [41] Q. Wang, W. Chen, *J. Energy Storage* **2022**, *51*, 104394.
- [42] C. T.-C. Wan, R. R. Jacquemond, Y.-M. Chiang, K. Nijmeijer, F. R. Brushett, A. Forner-Cuenca, *Adv. Mater.* **2021**, *33*, 2006716.
- [43] R. R. Jacquemond, C. T.-C. Wan, Y.-M. Chiang, Z. Borneman, F. R. Brushett, K. Nijmeijer, A. Forner-Cuenca, *Cell Rep. Phys. Sci.* **2022**, 100943.
- [44] H. Strathmann, K. Kock, *Desalination* **1977**, *21*, 241.
- [45] J. R. Werber, C. O. Osuji, M. Elimelech, *Nat. Rev. Mater.* **2016**, *1*, 16018.
- [46] G. R. Guillen, Y. Pan, M. Li, E. M. V. Hoek, *Ind. Eng. Chem. Res.* **2011**, *50*, 3798.
- [47] M. Radjabian, V. Abetz, *Progr. Polym. Sci.* **2020**, *102*, 101219.
- [48] A. J. Reuvers, *Ph.D. Thesis*, University of Twente, **1987**.

- [49] C. A. Smolders, A. J. Reuvers, R. M. Boom, I. M. Wienk, *J. Membr. Sci.* **1992**, 73, 259.
- [50] V. A. Kosma, K. G. Beltsios, *J. Membr. Sci.* **2012**, 407–408, 93.
- [51] D. R. Tree, T. Iwama, K. T. Delaney, J. Lee, G. H. Fredrickson, *ACS Macro Lett.* **2018**, 7, 582.
- [52] A. J. Reuvers, J. W. A. van den Berg, C. A. Smolders, *J. Membr. Sci.* **1987**, 34, 45.
- [53] A. J. Reuvers, C. A. Smolders, *J. Membr. Sci.* **1987**, 34, 67.
- [54] J. P. Craig, J. P. Knudsen, V. F. Holland, *Text. Res. J.* **1962**, 32, 435.
- [55] I. Cabasso, E. Klein, J. K. Smith, *J. Appl. Polym. Sci.* **1977**, 21, 165.
- [56] C. Kahrs, T. Gühlstorf, J. Schwellenbach, *J. Appl. Polym. Sci.* **2020**, 137, 48852.
- [57] H. Strathmann, K. Kock, P. Amar, R. W. Baker, *Desalination* **1975**, 16, 179.
- [58] A. Bourke, M. A. Miller, R. P. Lynch, X. Gao, J. Landon, J. S. Wainright, R. F. Savinell, D. N. Buckley, *J. Electrochem. Soc.* **2016**, 163, A5097.
- [59] T. V. Sawant, J. R. McKone, *J. Phys. Chem. C* **2019**, 123, 144.
- [60] P. Chen, M. A. Fryling, R. L. McCreery, *Anal. Chem.* **1995**, 67, 3115.
- [61] N. Pour, D. G. Kwabi, T. Carney, R. M. Darling, M. L. Perry, Y. Shao-Horn, *J. Phys. Chem. C* **2015**, 119, 5311.
- [62] X. Mao, F. Simeon, G. C. Rutledge, T. A. Hatton, *Adv. Mater.* **2013**, 25, 1309.
- [63] D. B. Schuepfer, F. Badaczewski, J. M. Guerra-Castro, D. M. Hofmann, C. Heiliger, B. Smarsly, P. J. Klar, *Carbon* **2020**, 161, 359.
- [64] J. Langner, M. Bruns, D. Dixon, A. Nefedov, Ch. Wöll, F. Scheiba, H. Ehrenberg, C. Roth, J. Melke, *J. Power Sources* **2016**, 321, 210.
- [65] Sigracet Whitepaper, <https://www.sglcarbon.com/pdf/SIGRACET-Whitepaper.pdf> (accessed: August 2022).
- [66] BMW and SGL to Triple Production Capacity at Moses Lake Carbon Fiber Plant with \$200M Expansion; World's Largest Carbon Fiber Plant, <https://www.greencarcongress.com/2014/05/20140509-sglacf.html> (accessed: August 2022).
- [67] L. Zeng, J. Sun, T. S. Zhao, Y. X. Ren, L. Wei, *Int. J. Hydrogen Energy* **2020**, 45, 12565.
- [68] C. Wan, A. Ismail, A. Quinn, Y.-M. Chiang, F. Brushett, *Chem. Eng. Ind. Eng.* **2022**, <https://doi.org/10.26434/chemrxiv-2022-3f18q>.
- [69] A. Sadezky, H. Muckenhuber, H. Grothe, R. Niessner, U. Pöschl, *Carbon* **2005**, 43, 1731.
- [70] W. H. Bragg, W. L. Bragg, *Proc. Roy. Soc. Lond. A* **1913**, 88, 428.
- [71] M. Thommes, K. Kaneko, A. V. Neimark, J. P. Olivier, F. Rodriguez-Reinoso, J. Rouquerol, K. S. W. Sing, *Pure Appl. Chem.* **2015**, 87, 1051.
- [72] H. R. Jiang, J. Sun, L. Wei, M. C. Wu, W. Shyy, T. S. Zhao, *Energy Storage Materials* **2020**, 24, 529.
- [73] X. You, Q. Ye, P. Cheng, *J. Electrochem. Soc.* **2017**, 164, E3386.
- [74] J. L. Barton, J. D. Milshtein, J. J. Hinricher, F. R. Brushett, *J. Power Sources* **2018**, 399, 133.
- [75] J. D. Milshtein, K. M. Tenny, J. L. Barton, J. Drake, R. M. Darling, F. R. Brushett, *J. Electrochem. Soc.* **2017**, 164, E3265.
- [76] M. MacDonald, R. M. Darling, *AIChE J.* **2018**, 64, 3746.
- [77] Q. He, J. Yu, Z. Guo, J. Sun, S. Zhao, T. Zhao, M. Ni, *e-Prime – Adv. Electric. Eng. Electron. Energy* **2021**, 1, 100001.
- [78] M. H. Gharahcheshmeh, C. T.-C. Wan, Y. A. Gandomi, K. V. Greco, A. Forner-Cuenca, Y.-M. Chiang, F. R. Brushett, K. K. Gleason, *Adv. Mater. Interfaces* **2020**, 7, 2000855.
- [79] A. K. Manohar, K. M. Kim, E. Plichta, M. Hendrickson, S. Rawlings, S. R. Narayanan, *J. Electrochem. Soc.* **2016**, 163, A5118.
- [80] C.-N. Sun, F. M. Delnick, D. S. Aaron, A. B. Papandrew, M. M. Mench, T. A. Zawodzinski, *ECS Electrochem. Lett.* **2013**, 2, A43.
- [81] J. Friedl, C. M. Bauer, A. Rinaldi, U. Stimming, *Carbon* **2013**, 63, 228.
- [82] D. D. Macdonald, *Electrochim. Acta* **2006**, 51, 1376.
- [83] J. Huang, Y. Gao, J. Luo, S. Wang, C. Li, S. Chen, J. Zhang, *J. Electrochem. Soc.* **2020**, 167, 166503.
- [84] I. Pivac, F. Barbir, *J. Power Sources* **2016**, 326, 112.
- [85] I. Pivac, B. Šimić, F. Barbir, *J. Power Sources* **2017**, 365, 240.
- [86] A. Kulikovskiy, *Electrochem. Commun.* **2022**, 140, 107340.
- [87] A. M. Pezeshki, R. L. Sacci, F. M. Delnick, D. S. Aaron, M. M. Mench, *Electrochim. Acta* **2017**, 229, 261.
- [88] C.-N. Sun, F. M. Delnick, D. S. Aaron, A. B. Papandrew, M. M. Mench, T. A. Zawodzinski, *J. Electrochem. Soc.* **2014**, 161, A981.
- [89] G. Kear, A. A. Shah, F. C. Walsh, *Int. J. Energy Res.* **2012**, 36, 1105.
- [90] T. V. Sawant, C. S. Yim, T. J. Henry, D. M. Miller, J. R. McKone, *Joule* **2021**, 5, 360.
- [91] K. E. Rodby, T. J. Carney, Y. Ashraf Gandomi, J. L. Barton, R. M. Darling, F. R. Brushett, *J. Power Sources* **2020**, 460, 227958.
- [92] X. Zhang, D. Zhang, Z. Xu, K. Zhang, Y. Zhang, M. Jing, L. Liu, Z. Zhang, N. Pu, J. Liu, C. Yan, *Chem. Eng. J.* **2022**, 439, 135718.
- [93] Q. Deng, Y. Tian, P. Ding, J. Yue, X.-X. Zeng, Y.-X. Yin, X.-W. Wu, X.-Y. Lu, Y.-G. Guo, *J. Power Sources* **2020**, 450, 227633.
- [94] M. Park, J. Ryu, Y. Kim, J. Cho, *Energy Environ. Sci.* **2014**, 7, 3727.
- [95] H. Giesche, *Part. Part. Syst. Character.* **2006**, 23, 9.
- [96] F. Moro, H. Böhni, *J. Colloid Interface Sci.* **2002**, 246, 135.
- [97] J. Schindelin, I. Arganda-Carreras, E. Frise, V. Kaynig, M. Longair, T. Pietzsch, S. Preibisch, C. Rueden, S. Saalfeld, B. Schmid, J.-Y. Tinevez, D. J. White, V. Hartenstein, K. Eliceiri, P. Tomancak, A. Cardona, *Nat. Methods* **2012**, 9, 676.
- [98] C. T.-C. Wan, D. López Barreiro, A. Forner-Cuenca, J.-W. Barotta, M. J. Hawker, G. Han, H.-C. Loh, A. Masic, D. L. Kaplan, Y.-M. Chiang, F. R. Brushett, F. J. Martin-Martinez, M. J. Buehler, *ACS Sustain. Chem. Eng.* **2020**, accsuschemeng.0c02427.
- [99] A. Alazmi, C. T.-C. Wan, P. M. F. J. Costa, F. R. Brushett, *J. Energy Storage* **2022**, 50, 104192.